



ESM Today 2016

Program

Saturday, February 27th

Keynote Speaker: Mike Erdman

Mr. Erdman is 1969 alumnus of the Engineering Science and Mechanics Department and today is the Director of the Leadership Development Program within the College of Engineering at Penn State. He is responsible for coordinating this world-class program, providing courses for students from across the university, and an optional minor for engineering students from the various engineering majors. He also instructs a multidisciplinary design course for Engineering Science and Mechanics. Mike and his wife operate Nicker Barker Farm where they breed golden retrievers, and he is retired from Lockheed Martin Corporation as the manager of fluid dynamics technology, where he was responsible for overseeing research and development in heat transfer, fluid dynamics, and two-phase flow.

Mr. Erdman is the founding president of the Engineering Science and Mechanics Alumni Advisory Board, President of the Penn State Engineering Alumni Society, and serves on the Industrial and Professional Advisory Council for the College. He has received the PSEAS Distinguished Service Award and the ESM Centennial Fellow Award from the College. He is a member of Parmi Nous, Phi Eta Sigma, Tau Beta Pi, and Theta Delta Chi and is on the board of the Centre County Chapter of the Alumni Association.

Schedule:

| | |
|------------------------|--|
| 8:30am-9:00am | Breakfast and registration |
| 9:00am-9:15am | Introduction by Dr. Todd |
| 9:15am-9:45am | Keynote Speaker- Mike Erdman |
| 9:45am-10:00am | Coffee Break |
| 10:00am-11:40am | Oral Presentations |
| 11:40am-1:15pm | Breakfast and Poster Exhibition |
| 1:15pm-1:30pm | Deliberation |
| 1:30pm | Awards Ceremony |



Oral Presentations:

| Room 114 EES | | Room 116 EES | |
|-----------------------|-----------------|--------------|-------------------|
| Faculty Judges | | | |
| Dr. Das | | Dr. Cheng | |
| Dr. Drapaca | | Dr. Lanagan | |
| Dr. Hamilton | | Dr. Ozbolat | |
| Dr. Tittmann | | Dr. Pitt | |
| | | Dr. Suliman | |
| Presenters | | | |
| 10:00-10:20 | Nitesh Nama | 10:00-10:20 | Christine Truong |
| 10:20-10:40 | Justin Kauffman | 10:20-10:40 | Zhangming Mao |
| 10:40-11:00 | Nick Labarbera | 10:40-11:00 | Yao Zhang |
| 11:00-11:20 | Adem Ozcelik | 11:00-11:20 | Aniruddh Vashisth |
| 11:20-11:40 | Joseph Nasr | 11:20-11:40 | Nitesh Nama |



ESM TODAY 2016

ORAL PRESENTATION ABSTRACTS

13th Annual Engineering Science and Mechanics Symposium



FEBRUARY 27, 2016

ENGINEERING SCIENCE AND MECHANICS (ESM) DEPARTMENT
THE PENNSYLVANIA STATE UNIVERSITY
212 EES BUILDING, SCE, PA 16803, USA

INVESTIGATION OF SHARP EDGE BASED ACOUSTOFLUIDIC MIXING

Nitesh Nama, Po-Hsun Huang, Francesco Costanzo, Tony Jun Huang

Department of Engineering Science and Mechanics
The Pennsylvania State University, Pennsylvania, USA

The ability to achieve rapid and homogeneous mixing at the microscale is essential for various lab-on-a-chip applications. Recently, we demonstrated a sharp-edge-based acoustofluidic micromixer [1], as well as investigation of the flow patterns around sharp edges [2]. Here, we extend our finite element numerical model, qualitatively validated by experimental results, to include the convection-diffusion equation and allow the presence of a background flow for investigating acoustic streaming based mixing phenomena. Our model utilizes a perturbation approach in conjunction with the convection-diffusion equation to characterize the effects of various geometrical and operational parameters for optimizing the performance of sharp-edge-based acoustofluidic micromixer.

Fig. 1 shows the schematic of the sharp-edge-based acoustofluidic micromixer consisting of a single-layer polydimethylsiloxane (PDMS) channel with sharp edges on its sidewall and bonded onto a glass slide. Upon the excitation of acoustic waves via a piezoelectric transducer, the sharp edges are oscillated, resulting in acoustic streaming. Fig. 2 shows the flow profile (a) before and (b) after the acoustic actuation. The resulting concentration profile from the mixing due to acoustic streaming is shown in Fig. 2(c).

We model the fluid motion using the compressible Navier-Stokes equations and the concentration profile with a convection-diffusion equation. To circumvent the numerical challenges associated with obtaining a direct solution of these equations [2], we utilize a perturbation approach to compute acoustic streaming flow along with the convection-diffusion equation to investigate the mixing. In contrast to the numerical model reported in [2], we allow for

the presence of a background flow. To confirm convergence of our numerical results, we performed a mesh convergence analysis by successively refining the mesh in the computational domain. Fig. 3(a) and (b) show the numerically computed flow profile before and after the acoustic actuation respectively, while Fig. 2(c) shows the concentration profile (experimental results). The numerically observed flow profile and concentration profile is in good qualitative agreement with the experimental results in Fig. 2. Fig. 4 shows the concentration profile for different values of the inlet flow velocity. A faster background flow results in suppression of the acoustic streaming effect, thereby yielding poorer mixing performance. Similarly, Fig. 5 shows the concentration profiles for different heights of the microchannel keeping the sharp edge height constant. As the height of the microchannel is increased, the performance of the acoustofluidic micromixer decreases for the same inlet flow velocity. However, the optimum performance of the micromixer can be achieved by tuning the acoustic power and inlet flow velocity.

In conclusion, we presented a numerical model to investigate acoustic mixing in sharp-edge-based acoustofluidic micromixer. We employ a perturbation analysis, while allowing for a background flow, to characterize the effect of geometrical and operational parameters on the mixing performance of the micromixer, and qualitatively validate the results with the experimental results. We believe that our computational model, while providing a better understanding of the mixing phenomena inside sharp-edge-based acoustofluidic micromixers, would be valuable in setting design criteria and optimization of many acoustofluidic-based lab-on-a-chip applications.

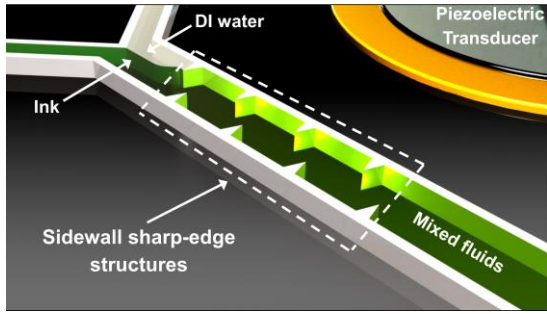


Fig. 1 Schematic of the acoustofluidic micromixer consisting of a polydimethylsiloxane (PDMS) microfluidic channel with sharp-edge structures on its side walls and a piezoelectric transducer. The sharp edges are designed to be of 250 μm height and a tip angle of 15° .

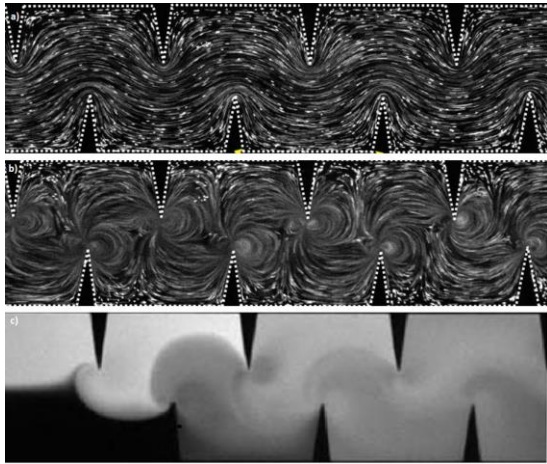


Fig. 2 Experimentally observed trajectories of 1.9 μm diameter beads (a) before and (b) after the actuation of acoustic waves, where acoustic streaming is observed around the tips of the sharp-edges. (c) Concentration profile inside the acoustofluidic micromixer showing the device's mixing performance. An inlet flow rate of 1 $\mu\text{l}/\text{min}$ was employed.

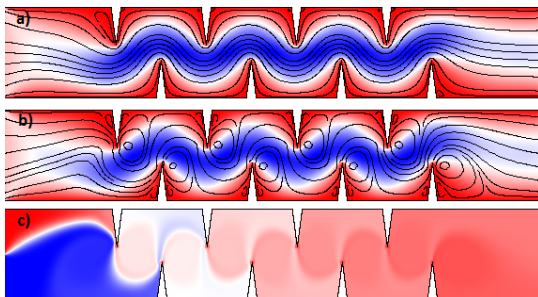


Fig. 3 (a) Numerically simulated trajectories of 1.9 μm diameter beads (a) before and (b) after the actuation of acoustic waves, showing the acoustic streaming around the tips of sharp-edges. (c) Numerically obtained concentration profile showing good

qualitative match with the experimentally observed concentration profile in Fig. 2(c).

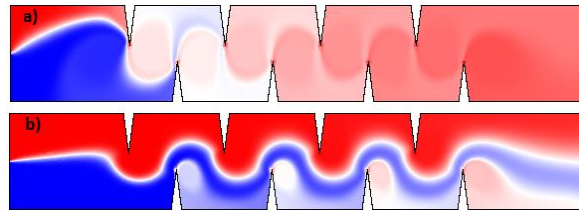


Fig. 4 Numerically obtained concentration profiles for different inlet flow rates at same input power: (a) $Q_{in} = 1 \mu\text{l}/\text{min}$ and (b) $Q_{in} = 5 \mu\text{l}/\text{min}$. For faster flow rates, incomplete mixing is observed necessitating the use of higher input power or larger mixing length.

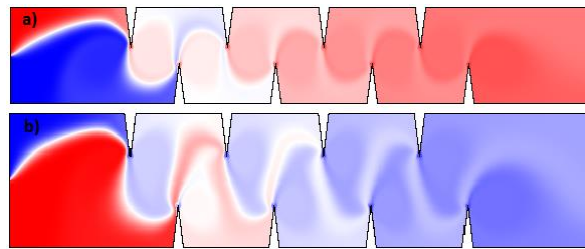


Fig. 5 Numerically obtained concentration profiles for different channel heights with same inlet flow rates and input power: (a) $H = 600 \mu\text{m}$, and (b) $H = 800 \mu\text{m}$. The acoustofluidic micromixer shows potential for mixing in even wider channels with use of either higher power or a larger mixing length.

REFERENCES:

1. P. H. Huang, Y. Xie, D. Ahmed, J. Rufo, N. Nama, Y. Chen, C. Y. Chan, and T. J. Huang, *Lab on a Chip*, Vol. 13, pp. 3847-3852, 2013.
2. N. Nama, P. H. Huang, T. J. Huang, F. Costanzo, *Lab on a Chip*, Vol. 14, pp. 2824-2836, 2014.

Coupled Overset Meshing and Hybridizable Discontinuous Galerkin Finite Elements

JUSTIN KAUFFMAN ADVISED BY DR. JONATHAN PITT

The Pennsylvania State University,

Department of Engineering Science and Mechanics, University Park, PA-16802

Computational simulations generally rely on both the discretization of the physical domain under study and the mathematical model of the problem. The discretization techniques implemented for this research are overset meshes for the former and the hybridizable discontinuous Galerkin (HDG) finite element method for the latter. Coupling these discretization techniques provides viable competition for overset finite volume solvers in the computational fluid dynamics (CFD) community.

The discretization of the physical geometry into polygonal volumes is called a *mesh*. As problems grow in complexity, it is increasingly more difficult to discretize the geometry with a single mesh [1]. An overset mesh refers to a collection of meshes, for a particular geometry, that are allowed to overlap such that a single spatial point can be contained in multiple meshes. Having the capability of overlapping meshes reduces the complexity of the generated meshes, but simultaneously increases the computational difficulty. Implementation of overset mesh methods needs to address reduction of orphan points, hole cutting, and grid communication. Orphan points are observed when there is no corresponding donor cell in an overlapped region of the domain. One way that orphan points can be generated is through hole cutting, which removes cells that are contained within a solid-body [2] and can cause voids in the discretized domain. Several commercial overset grid assemblers have addressed the issue of hole cutting. PEGASUS5 [3] implements a nearly automatic hole cutting algorithm, and SUGGAR++ [4] utilizes immersed boundaries in small gaps caused by hole cutting to eliminate the generated orphan points. Finally, communication between the overset meshes is necessary. Information is passed from a donor mesh to the overlapped points

on the receiving mesh through interpolation schemes [5]. In finite volume overset methods it is necessary to have more rows of cells with overlap for higher order solutions [6].

The finite element method is a discretization technique for a chosen mathematical model (partial differential equation). Continuous Galerkin (CG) finite elements were developed to solve structural mechanics problems in the 1950's [7]. These traditional finite elements have since been optimized to give accurate solutions to a variety of engineering problems. Discontinuous Galerkin (DG) methods were introduced to mimic the locally conservative nature of finite volume methods [8] which is not ensured for Eulerian reference frames in CG methods. Unfortunately, DG methods experience an 'explosion' of degrees of freedom (DoF) since there are duplicate DoF on the boundaries between elements. A hybridization process was introduced to alleviate the large number of globally coupled DoF at element interfaces [9]. Hybridization of a finite method, in general, introduces new unknowns on element interfaces that are used to reduce the problem size or enrich the function space of the solution. The HDG method greatly reduces the global system and reformulates the governing equations such that volumetric DoF are eliminated in favor of the smaller set of surface/face DoF.

Results for convection-diffusion and elastostatics problems, as well as preliminary results for Stokes flow, are presented for the coupled overset HDG system with *arbitrary* overlap between meshes. Applications, such as that shown in Fig. 1 for elastostatics, comparing non-overset HDG and the coupled overset HDG system are discussed. More analysis and numerical experiments need to be performed to validate the coupling between the two techniques.

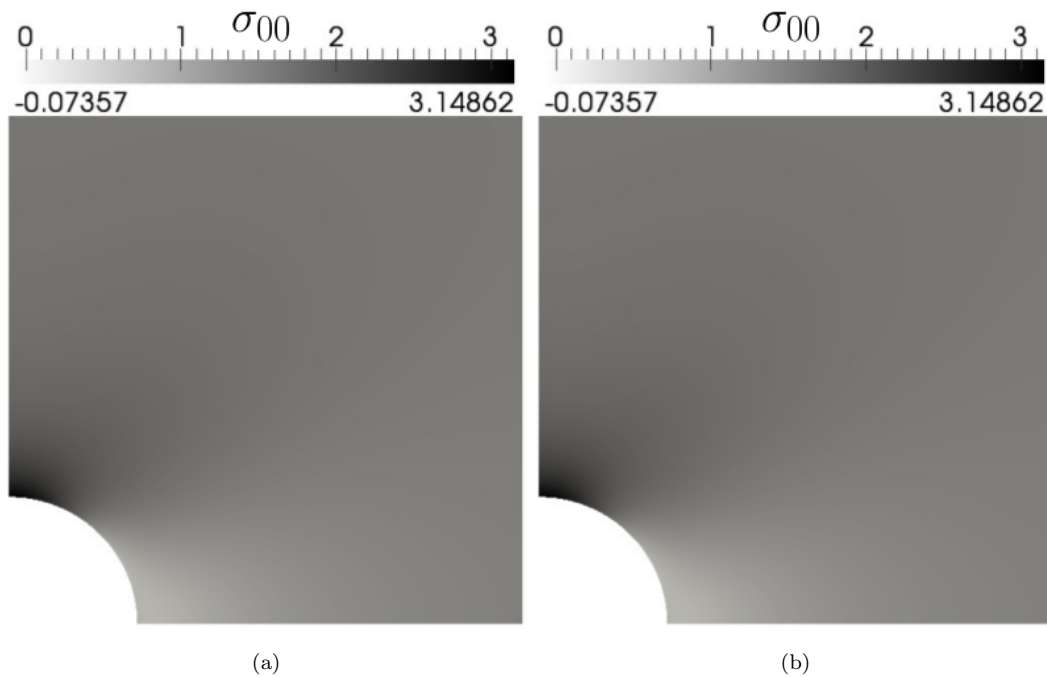


Figure 1: Solution of rectangle plate with circular hole for a (a) single mesh and (b) an overset mesh.

References

- [1] M. C. Galbraith, J. A. Benek, P. D. Orkwis, and M. G. Turner, “A Discontinuous Galerkin Chimera scheme,” *Computers & Fluids*, vol. 98, pp. 27–53, 2014.
- [2] S. E. Sherer and J. N. Scott, “High–Order compact finite–difference methods on general overset grids,” *Journal of Computational Physics*, vol. 210, pp. 4459–496, 2005.
- [3] W. M. Chan, “Overset grid technology development at NASA Ames Research Center,” *Computer & Fluids*, vol. 38, pp. 496–503, 2009.
- [4] R. W. Noack, D. A. Boger, R. F. Kunz, and P. M. Carrica, “Suggar++: An Improved General Overset Grid Assembly Capability,” in *19th AIAA Computational Fluid Dynamics*, 2009.
- [5] T. K. Sengupta, V. Suman, and N. Singh, “Solving Navier–Stokes equation for flow past cylinders using single–block structured and overset grids,” *Journal of Computational Physics*, vol. 229, pp. 178–199, 2010.
- [6] N. F. Foster and R. W. Noack, “High–Order Overset Interpolation within an OVERFLOW Solution,” in *50th AIAA Aerospace Sciences Meeting including the New Horizons Forum and Aerospace Exposition*, 2012.
- [7] F. Auricchio, F. Brezzi, and C. Lovadina, “Mixed finite element methods,” *Encyclopedia of computational mechanics*, 2004.
- [8] B. Cockburn, “Discontinuous galerkin methods,” *ZAMM–Journal of Applied Mathematics and Mechanics/Zeitschrift für Angewandte Mathematik und Mechanik*, vol. 83, pp. 731–754, 2003.
- [9] B. Cockburn and J. Gopalakrishnan, “Incompressible Finite Elements via Hybridization. Part I: The Stokes System in two Space Dimensions,” *SIAM Journal on Numerical Analysis*, vol. 43, pp. 1627–1650, 2005.

Model Order Reduction for Incompressible Navier-Stokes Simulations

NICHOLAS LABARBERA ADVISED BY DR. JONATHAN PITT

Department of Engineering Science and Mechanics, Penn State, PA-16802, USA

Numerically simulating fluid flow is very computationally expensive, and can be a bottleneck in the engineering design process. For this reason, there is a need for developing model reduction techniques that can reproduce the physics of the system with minimal computational resources. Even when sufficient computational resources are available, it is still beneficial to have a model that can be computed in a fraction of the time.

One model reduction technique is to replace the locally supported basis vectors typically used in the finite element method with a significantly smaller number of globally supported basis vectors [1]. By solving the system's governing equations in a lower dimensional space, large computational savings are reaped. The caveat is that properly choosing these new global basis vectors is crucial to the accuracy and the stability of the reduced-order model.

Proper orthogonal decomposition (POD) is one way of choosing optimal basis vectors in the L^2 norm [2]. The technique takes as input a set of snapshots of a full-order simulation. It then outputs an orthonormal set of basis vectors that minimize the L^2 error between the space spanned by the outputted basis vectors and the original snapshots [2]. These globally supported basis vectors can be thought of as the most energetic modes of the system [3]. The modes of the system can then be used in conjunction with a numerical equation solving technique such as the Galerkin method to solve the system with different inputs than was used

to make the original snapshot set [3]. Using the modal basis vectors for different inputs is similar to using a different mesh but with a different set of inputs.

Two different cases are used to demonstrate the computational savings and accuracy of this model reduction technique. The first is a lid-driven cavity with Dirichlet conditions on the boundaries. The second case is an object in channel flow shedding vortices. For both examples, simulations were run while varying inflow conditions and number of modes. Comparisons are made between the reduced-order model and the full-order model. The results show that the POD/Galerkin model reduction technique can be a viable option for reducing the computational burden of solving incompressible Navier-Stokes equations.

References

- [1] P. Holmes, J. L. Lumley, and G. Berkooz, *Turbulence, coherent structures, dynamical systems and symmetry*. Cambridge university press, 2012.
- [2] A. Chatterjee, "An introduction to the proper orthogonal decomposition," *Current Science*, vol. 78, p. 8, April 2000.
- [3] J. Burkardt, M. Gunzburger, and H.-C. Lee, "Pod and cvt-based reduced-order modeling of navier-stokes flows," *Computer Methods in Applied Mechanics and Engineering*, vol. 196, no. 1-3, pp. 337 – 355, 2006.

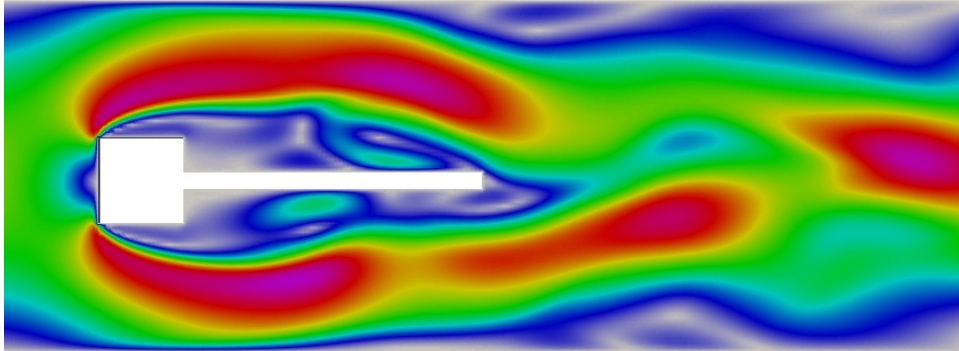


Figure 1: A snapshot of velocity magnitude from the full-order simulation of a rigid object shedding vortices in channel flow. Numerous snapshots of the full-order model flow field such as this was used to derive an empirical basis for the simulations.

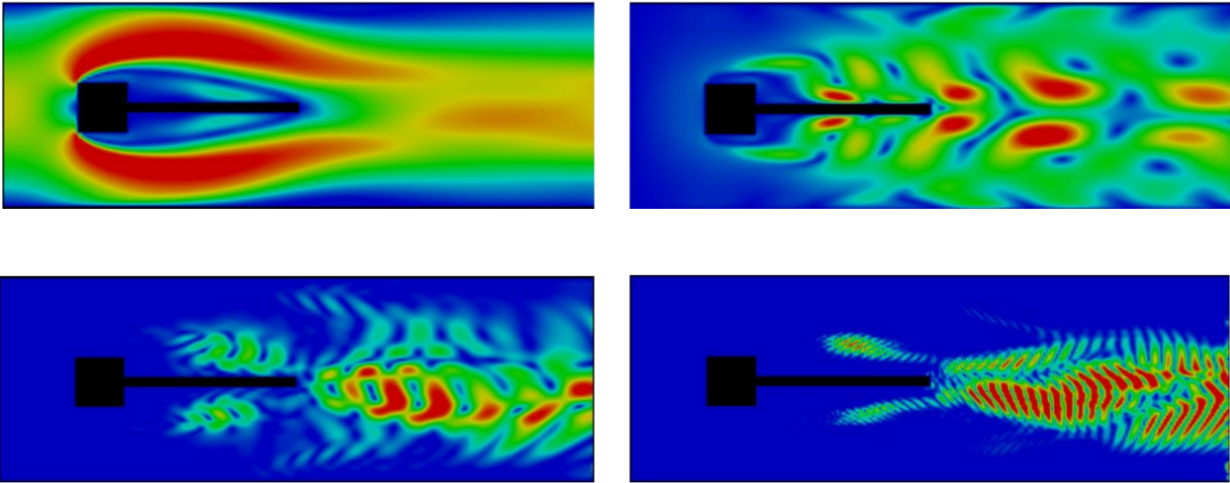


Figure 2: Various modes of the system that were derived from snapshots of the full-order flow field shown in Figure 1. The modes are globally supported basis vectors that can be used with the Galerkin method to form a reduced-order model of the system that runs in a fraction of the time.

ROTATIONAL MANIPULATION OF SINGLE CELLS AND ORGANISMS USING ACOUSTIC WAVES

A. Ozcelik and T. J. Huang

Department of Engineering Science and Mechanics, Penn State, PA-16802, USA

Precise rotational manipulation of particles, cells, and multicellular organisms is an essential capacity in biotechnology that impacts various disciplines including single-cell analysis[1], drug discovery[2], and organism studies[3]. Providing three-dimensional (3D) interrogation, rotational manipulation can reveal hidden genetic, cellular, and structural details which are vital in small organism phenotyping, screening, and microsurgery and which are not visible in typical translational manipulation. Although several techniques have been established for the translational manipulation of particles and cells, there is no existing method that has demonstrated the capacity to rotate small model animals (such as *C. elegans*) or cells on a single chip.

In this work, we describe an acoustofluidic rotational manipulation (ARM) method, which utilizes steady acoustic microstreaming vortices created by the oscillatory motion of air microbubbles trapped in a microfluidic channel (Figure 1). The oscillatory motion is driven by the application of a low-power acoustic field. The ARM method presented here represents the first acoustic-based rotational manipulation approach to rotate biospecimen. This method is extremely versatile. Its operation is independent of the samples' intrinsic properties. It allows effective and precise rotation of specimens over a wide range of sizes, shapes, and properties. In addition, compared to optical, magnetic, or electric field based rotational manipulation methods, ARM is both extremely simple and practical. The entire operation requires only a single-layer polydimethylsiloxane (PDMS) channel and a simple, low-cost piezo transducer which can be integrated to existing microfluidic platforms. Using ARM, we have demonstrated for the first time, on-chip rotation of *C. elegans*, a valuable and frequently used model organism for elucidating the molecular mechanisms underlying human diseases.

Our ARM technology shows significant advances in biocompatibility and versatility beyond existing rotational manipulation methods. We have demonstrated the biocompatibility of our method by conducting a HeLa cell viability test, which resulted in a ~99.2% survival rate for the cells after

experiencing acoustic field for one to two minutes. The ARM technology provides unique advantages for imaging a model organism such as *C. elegans*. During investigations of the ALA neuron dendrites, imaging in general was difficult due to overlapping of GFP patterns; rotation of the worm permitted acquisition of distinct dendrites images in a single animal and allowed access to the neuronal network of the organism. This feature holds great promise for *in vivo* laser microsurgery studies applied in axon regeneration processes, where you can damage multiple neurons at a time and later analyse their regeneration properties with ease. We used our method to examine the composition and structure of the *C. elegans* vulva (Figure 2). Rotational manipulation allowed us to categorize mutant worms by analysing the defective cell shape and size comprising the vulval rings. Specimen rotation using ARM is precise, rapid, and more importantly, controllable, thus photobleaching becomes less challenging for fluorescent samples. Furthermore, dynamic rotational positioning and rapid identification of the defective cellular structures can be potentially coupled with on-chip model animal sorting applications. It is also important to note that the ARM chip costs less than \$1 in bulk fabrication. The permanent instrument, which includes compact, custom-designed electronics, can be manufactured for under \$100. With this inexpensive setup, even low-cost fluorescent microscopes can be used to obtain 3D imaging capability, which makes 3D imaging accessible to many low-budget laboratories around the world that do not have access to confocal microscopy facilities. The ARM method can be extended to other small organisms by simple design modifications of the microfluidic devices. The ARM method offers rapid and accurate angular adjustment of the cells and organisms. Given the growing use of organism-on-chip tools for investigating small animals, our method is valuable in the field of bioengineering, biophysics, medicine, and developmental biology.

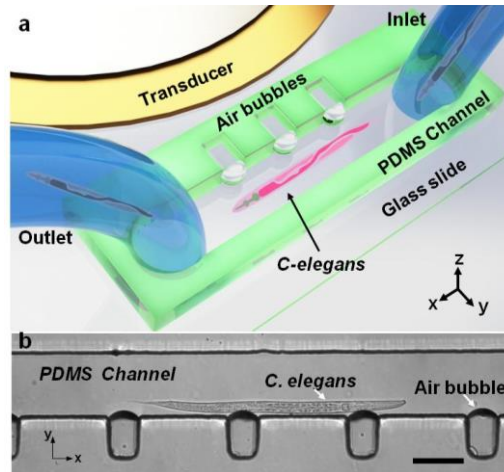


Figure 1. Design and operation of the acoustofluidic rotational manipulation (ARM) device. (a) A schematic of the experimental setup. The piezoelectric transducer that generates acoustic waves is placed adjacent to the microfluidic channel. The acoustic waves actuate air microbubbles trapped within sidewall microcavities. (b) An optical image showing a mid-L4 stage *C. elegans* trapped by multiple oscillating microbubbles. Scale bar = 100 μm .

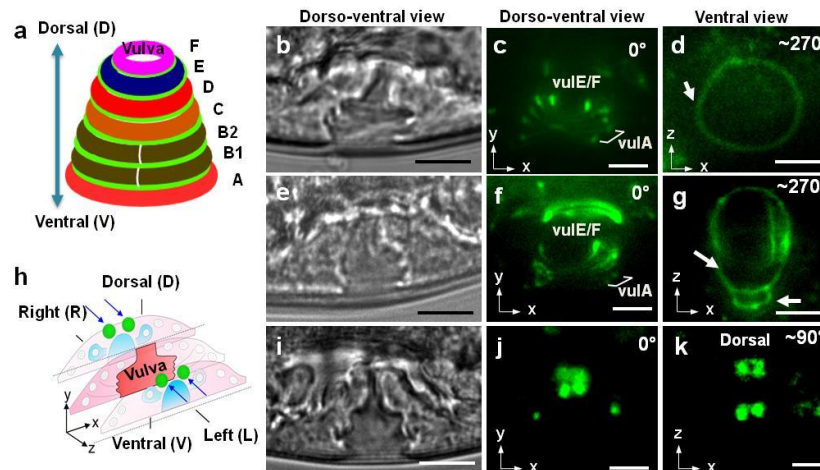


Figure 2. Toroid formation and cell position during *C. elegans* reproductive system morphogenesis. (a) A schematic of vulva structure of a *C. elegans* showing 7 concentric toroidal rings, VulA to VulF. Digital image of a vulva of (b,i) a wild-type animal and (e) an *nhr-25(RNAi)* animal. *AJM-1::GFP* adherens junction rings in (c) a wild-type and (f) an *nhr-25(RNAi)* animal acoustically driven along the dorso-ventral axis. (d) The ventral view of an ARM rotated worm showing shape and size of border of vulA in wild-type and (g) in *nhr-25(RNAi)* animals. In the *nhr-25(RNAi)* animal, the vulA border is expanded laterally and abnormal adherens junctions (arrows) were seen. (h) A schematic of vulva epithelial cell positions along the left and right axis. Two VulF cells on the right and two on the left shown in green. (j) Dorso-ventral view shows two GFP+ cells. (k) Ventral view obtained through ARM clearly shows four GFP+ cells. Scale bars = 10 μm .

REFERENCES

- [1] I. Pushkarsky, Y. Lyb, W. Weaver, T.-W. Su, O. Mudanyali, A. Ozcan, and D. Di Carlo, "Automated single-cell motility analysis on a chip using lensfree microscopy," *Sci. Rep.*, vol. 4, Apr. 2014.
- [2] A. J. Chung, Y. S. Huh, and D. Erickson, "A robust, electrochemically driven microwell drug delivery system for controlled vasopressin release," *Biomed. Microdevices*, vol. 11, no. 4, pp. 861–867, Aug. 2009.
- [3] I. de C. Cáceres, N. Valmas, M. A. Hilliard, and H. Lu, "Laterally orienting *C. elegans* using geometry at microscale for high-throughput visual screens in neurodegeneration and neuronal development studies," *PLoS One*, vol. 7, no. 4, p. e35037, Jan. 2012.

Phase control of RF Sputtered SnS_x with Post-Deposition Annealing for Photovoltaic Device Applications

J. R. Nasr and M. W. Horn

Department of Engineering Science and Mechanics, Penn State, PA-16802, USA

A solar cell is an electronic device that converts sunlight into electrical currents using the photoelectric effect. Basically, light shining on the solar cell produces both a current and a voltage to generate electric power. In order for a solar cell to achieve photovoltaic energy conversion, three crucial steps are needed: 1) the absorption of light, 2) separation of the generated charge carriers of opposite types (electrons and holes), and 3) a circuit connected to a load [1].

Up until now, various types of solar cells have been suggested and developed: 1) inorganic solar cells incorporating inorganic semiconductor materials and next generation thin film solar cells, 2) dye-sensitized solar cells (DSSCs) consisting of light-absorbing dye molecules, oxidized semiconductor material, redox electrolyte, and catalyzed counter electrodes and 3) organic solar cells with light-absorbing polymers and conductive polymers [1]. Solar cells with thin film absorber layers, which have efficiencies of 20.4% and 20.8%, have been produced using CdTe and CuIn_xGa_{1-x}Se₂ (CIGS), respectively [2].

SnS-based solar cells have the potential to achieve 24% efficiencies based on the optoelectronic properties of SnS_x [3], however, the best reported device using SnS_x produced less than 5% efficiency [4]. SnS is a semiconductor material with reported direct and indirect band gaps of 1.33 to 1.55 eV and 1.07 to 1.39 eV respectively. It has a high absorption coefficient of $>10^4 \text{ cm}^{-1}$ and possesses various other ideal physical properties; it is cost efficient, non-toxic, and abundant in the Earth's crust.

For practical and economical solar cells, scientists and engineers rely on the use of thin film technology because it reduces the amount of active material in a cell. Several thin film fabrication methods to produce these films have been reported [5]. SnS synthesis studies have focused on low-temperature processing techniques, which in general result in complete sulfur utilization. However, wet chemistry techniques are generally not favorable for large-scale manufacturing of PV modules. Sputter deposition is known to produce high-quality films and is also easily scalable. With the help of the plasma, extra energy is provided to the deposition precursors, which also offers more film-growth control. Unfortunately, only a few studies have investigated sputtered SnS_x, but none have fully explored the parameter space.

The depositions in this study were made using a radio frequency (rf 13.56 MHz) magnetron sputtering

system oriented in a downward vertical geometry. Previous studies of SnS_x films made by sputtering used a pure SnS target, however the films showed sulfur deficiency, which has deleterious effects on the electronic properties of the film. In order to decrease sulfur vacancies, a SnS₂ target is used in this investigation as a way to ensure the desired sulfur content and electrical properties [6] (Figure 1). With the help of a roughing pump connected to the chamber, low vacuum (~50 mTorr) was achieved. After roughing the chamber to low vacuum, the chamber was pumped down with a turbomolecular pump to achieve medium vacuum conditions of $<2 \times 10^{-6}$ Torr. In order to minimize film contamination, depositions were spaced at least 12 hours apart to ensure minimal oxygen contamination.

Several reports in the literature suggest that by using proper top or bottom contacts and a matching heterostructure material such as CdS, one could increase the efficiency of the device to approximately 10%. Cells of this type could potentially cost less than \$0.50/Watt. We have been investigating contacts to SnS, particularly those that have high work function (Pd and Pt) – examined as both top and bottom. Initially, two optimal pathways are investigated for obtaining an n-type as well as a p-type SnS material by adjusting annealing conditions with the intent of evaluating a pseudo-homojunction photovoltaic solar cell (Figure 2). Depositions were conducted at a fixed power (115 W), pressure (10 mTorr), and time (10 minutes). A series of anneals were executed at temperatures ranging from 300°C to 400 °C, lasting from 10 to 60 minutes.

These films were examined using X-ray diffraction, field emission scanning electron microscopy (FESEM), UV-Vis spectrophotometry, hot probe, four-point probe, and transmission line measurement (TLM/CTLTM).

Future work will entail fabricating a heterostructure with p-type SnS_x with an n-CdS layer (provided by NREL). These n-CdS were deposited onto both FTO and a bi-layer FTO/TO glass substrate. Variables in the CdS films include: glass type, oxygen content, indium doping, CdS thickness, and CdCl₂ treatment (Figure 3).

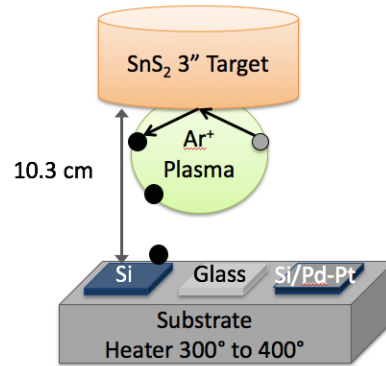


Figure 1: Sputtering technique.

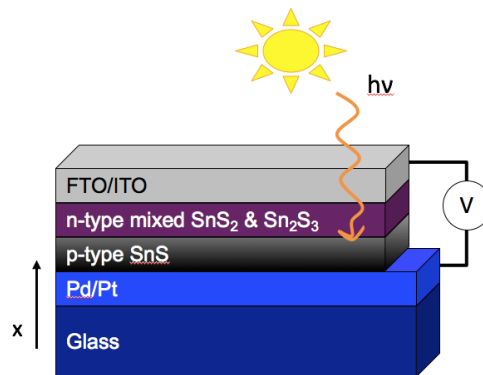


Figure 2: Pseudo-homojunction photovoltaic cell.

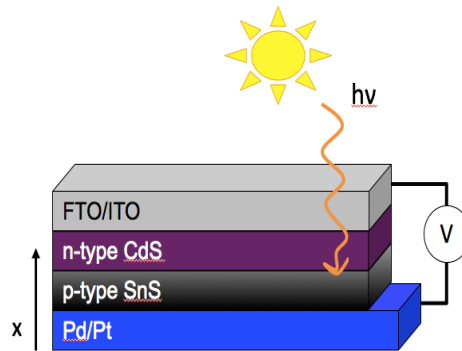


Figure 3: Heterojunction n-type CdS/p-type SnS.

REFERENCES

1. S. Fonash, Solar cell device physics, 2nd ed., Burlington: Elsevier, 2010.
2. "NREL: National Renewable Energy Laboratories," 27 June 2014. [Online]. Available: http://www.nrel.gov/ncpv/images/efficiency_chart.jpg. [Accessed 30 June 2014].
3. J. L. Loferski, "Theoretical Considerations Governing the Choice of the Optimum Semiconductor for Photovoltaic Solar Energy Conversion," *J. App. Phys.*, vol. 7, no. 27, p. 777, 1956.
4. Andrade-Arvizu, J.A., Courel-Piedrahita, M. & Vigil-Galán, O. 2015, "SnS-based thin film solar cells: perspectives over the last 25 years", *Journal of Materials Science: Materials in Electronics*, vol. 26, no. 7, pp. 4541-4556.
5. P. Sinsermsuksakul, L. Sun, S. W. Lee, H. H. Park, S. B. Kim, C. Yang and R. G. Gordon, "Overcoming Efficiency Limitations of SnS-Based Solar Cells," *Adv. Energy Mater.*, vol. 4, no. 15, p. 1400496., 2014.
6. Banai, R.E., Cordell, J.C., Lindwall, G., Tanen, N.J., Shang, S.-, Nasr, J.R., Liu, Z.-, Brownson, J.R.S. & Horn, M.W. 2016, "Control of Phase in Tin Sulfide Thin Films Produced via RF-Sputtering of SnS₂ Target with Post-deposition Annealing", *Journal of Electronic Materials*, vol. 45, no. 1, pp. 499-508.

Feeling the Flow: Optical Diagnostic Techniques to Characterize Turbulent Behavior

Christine Truong^{1,2} and Jeff Harris²

¹ Department of Engineering Science and Mechanics, Penn State, PA 16801

² Garfield Thomas Water Tunnel, Applied Research Laboratory, Penn State PA 16801

Particle Image Velocimetry (PIV) and Particle Shadow Velocimetry (PSV) are two measurement techniques used to quantify information about velocity fields in fluid flow. The goal is to use velocity fields to extract turbulent integral length scales, which are the characteristic lengths of the largest eddies in the flow. Length scales are critical values to most turbulence models.

Using PIV, quantities of interest (such as 2-component velocities) can be optically measured without placing obstructive probes in the flow. A pulsed laser is placed so that a laser sheet illuminates a plane in the fluid. Illuminated particles in the flow reflect this light into a camera. Using a cross-correlation algorithm, the particle displacements are computed. Using the displacements of these particles and knowing the time between frames, the velocity field can be digitally reconstructed and a length scale in the plane of the illumination can be extracted from the velocity field.

PSV is a variant of PIV, except that PSV is acquired using a light source that shines through the optical axis directly into the camera. The camera captures light that is not shadowed by the particles. Tracking the shadows provides displacement information that are used to reconstruct a velocity field. PSV allows the expensive, high-power laser to be replaced with an inexpensive, low-power and safer light source, such as an LED [1]. The comparison of PIV and PSV is shown in Fig. 1.

The discussed methods so far yield single plane velocity fields from PIV and PSV; however, multiplanar information can easily be obtained using PSV [2]. Two distinct measurement planes along the optical axis of the flow can be simultaneously measured using a multicolor LED, a dichroic mirror, and two cameras. The two colors of the LED illuminate the optical axis and either pass through or are reflected by the dichroic mirror, and enter one of two cameras. Standard PIV algorithms can then be used to calculate velocity fields. The velocity fields in these two distinct planes can be used to calculate length scales in the direction *between* the planes, instead of in the plane of the illumination.

Velocity fields can be used to calculate integral length scales using

$$l(\mathbf{x}, t) \equiv \frac{3}{16} \int_0^\infty \frac{R_{ii}(\mathbf{x}, t; \mathbf{r})}{k(\mathbf{x}, t)} d\mathbf{r}$$

where \mathbf{x} is some point in the flow, t is time, \mathbf{r} a displacement vector from \mathbf{x} and r the magnitude of that vector, $R_{ii}(\mathbf{x}, t; \mathbf{r})$ a two-point correlation tensor between the fluctuating velocities at \mathbf{x} and $\mathbf{x}+\mathbf{r}$, and $k(\mathbf{x}, t)$ the turbulent kinetic energy tensor calculated with no displacement:

$$R_{ij}(\mathbf{x}, t; \mathbf{r}) = \overline{u'_i(\mathbf{x}, t)u'_j(\mathbf{x} + \mathbf{r}, t)}$$

$$k(\mathbf{x}, t) = \frac{1}{2} R_{ii}(\mathbf{x}, t; \mathbf{0})$$

Length scales can be calculated using a spatial correlation, as shown above, or using a temporal correlation [3].

Experiments were conducted inside the 11.2-inch diameter glycerin tunnel in Penn State's Applied Research Laboratory. Glycerin properties, such as density, viscosity, Reynolds number, flow velocity etc. are determined by the operating temperature (100 °F). A 1.1-meter long clear acrylic test section is located in the glycerin tunnel to optically observe fully-developed turbulent flow behavior. Pressure taps are located upstream of the test section to measure the pressure gradient allowing the friction velocity to be measured. LaVision's DaVis 8.2.3 was used to analyze flow fields captured by a Vision Research Phantom v311 camera and generate a corresponding velocity field. MATLAB was used to post-process velocity fields and calculate statistics and length scales. Velocity statistics are presented for single plane PIV and PSV. Fig. 2 shows that the velocity profile for single-plane PSV is in agreement with PIV, previous measurements, and empirical models. Multiplane PSV and integral length scales are forthcoming, with a preliminary velocity correlation extracted from single-plane PIV shown in Fig. 3. The integral of this curve is the length scale of the flow.

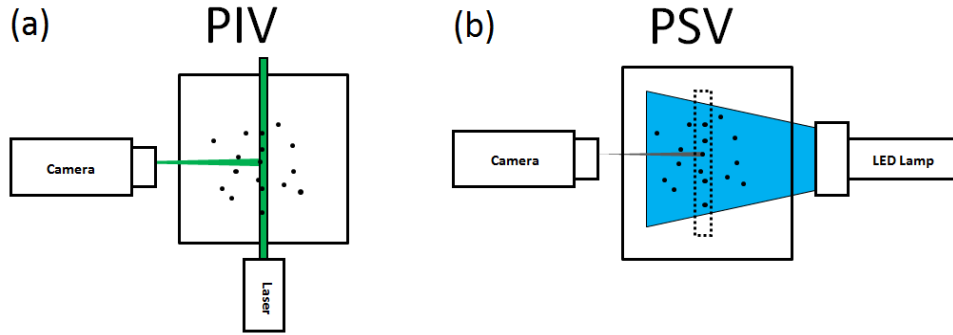


Figure 1: A comparison of (a) a PIV setup and (b) a PSV setup. In PIV, the optical plane is illuminated by the laser and particles in the flow reflect light into the camera, appearing as bright spots. In PSV, the optical axis is illuminated by the LED and particles in the flow absorb this light, so they appear as dark spots. [2]

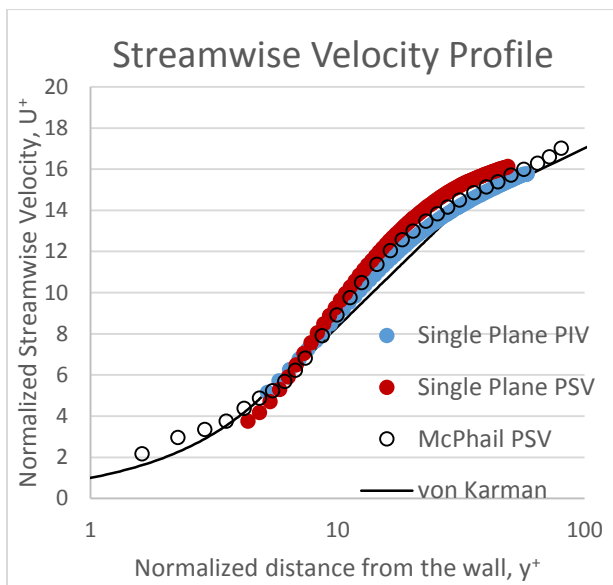


Figure 2: The measured streamwise velocity profile as a function of distance from the wall, plotted against previous measurements by McPhail [2], and the empirical von Karman velocity profile. All values have been nondimensionalized to allow for comparison.

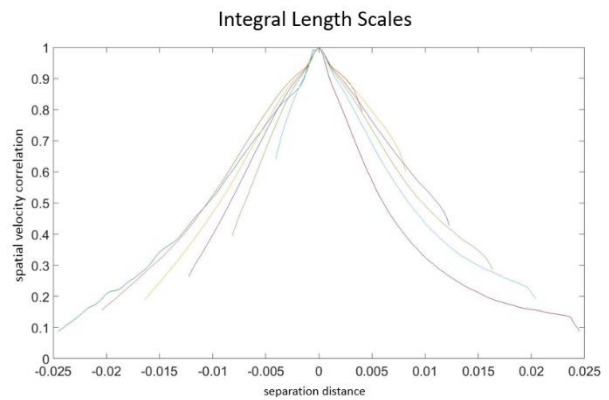


Figure 3: A spatial correlation plot calculated using single plane PIV. The integral of this curve is the desired length scale.

ACKNOWLEDGEMENTS

I would like to thank my group members Kyle Sinding and Steven Hinkle, and their advisors Michael Krane and Rhett Jefferies.

REFERENCES

- [1] J. Esteveadoral, and L. Goss, "PIV with LED: Particle Shadow Velocimetry (PSV)" *American Institute of Aeronautics and Astronautics 43rd meeting* (2005)
- [2] M. McPhail, et al., "Correcting for Color Crosstalk and Chromatic Aberration in Multicolor Particle Shadow Velocimetry." *Meas. Sci. Technol.* 26.2 (2015) 025302.
- [3] D. C. Wilcox, *Turbulence Modeling for CFD Third Edition*, DCW Industries (2006)
- [4] A. A. Fontaine, and S. Deutsch, "Three-component, time-resolved velocity statistics in the wall region of a turbulent pipe flow" *Experiments in Fluids*, 18(3), 168-173. (1995)

Formation of colloid pattern in bubble-pen lithography

Zhangming Mao and Tony Jun Huang

Department of Engineering Science and Mechanics, Penn State, PA-16802, USA

Lithography¹ is one of the main strategies that apply in nanofabrication. Photolithography has remained as driving force for semiconductor industry. However, its resolution is reaching an ultimate limit. E-beam lithography and ion-beam lithography feature high resolution and arbitrary patterning, however, are limited by high cost and low throughput. Recently, a versatile lithography technique known as bubble-pen lithography² (BPL) was developed for arbitrary patterning of colloidal particles on solid-state substrates using optothermally generated microbubble. It provides an alternative way for nanofabrication in a manner of low cost and high throughput. To understand the mechanism of formation of colloid in BPL, numerical simulations were done to gain insight of this phenomena.

In BPL technology a microbubble is generated on a plasmonic substrate consisting of AuNIs via shining laser on. Once microbubble appears, micro-sized PS beads move towards the microbubble and are trapped on it. The process is illustrated in Fig. 1a. Through numerical simulation, the temperature distribution around the microbubble can be found, as shown in Fig. 1b, indicating that there exists a temperature gradient from the bottom of microbubble to the top. Due to the temperature gradient, the surface tension along the microbubble/solution interface also present a gradient, which can induce Marangoni stress at the interface (Fig. 1a). Both of the temperature gradient and Marangoni stress drive a convective stream that flows from bottom to top, and drags PS beads moving towards the microbubble. When the PS beads contact with the microbubble, they are immobilized and trapped on the microbubble via the surface tension force and the pressure difference between the stream inside the bubble and fluid outside the bubble (insert of

Fig. 1a). Experiment results of PS beads trapping is shown in Fig. 1d².

Fig. 2a shows the optical micrographs of the variable microbubbles generated under the light illumination with different power densities. As shown in Figs. 2b and c, the 540 nm PS beads can be immobilized on the substrate by the bubbles, leading to the different patterns. At the lowest optical power density, three PS beads form a cluster with 2D configuration. When the power density increases, a large bubble with a diameter of $>3 \mu\text{m}$ leads to a three-dimensional (3D) hollow structure of the beads on the substrate (Fig. 2d).²

CFD simulations were done to gain an insight into the formation mechanism of the 3D hollow structures of PS beads. As illustrated in Figs. 2e-g, the convective flow drags the beads towards the bubble/substrate interface and generates the 3D hollow structure by the “bottom-up” layer-by-layer stacking. Such a stacking process is enabled by the fact that the initially trapped beads at the bubble surface block the Marangoni stress there and modify the convective flow distributions in a way that the convective flow points toward the upper part of the bubble. However, a reverse convective flow occurs when the bubble traps five layers of beads (Fig. 2g). The reverse flow pushes the free beads in suspension away from the trapped ones. The velocity around the microbubble is 4-5 orders of magnitude lower than that before the beads are trapped, indicating that the trapping process stops once the bubble surface is covered with beads. The 3D hollow structures are generated when the microbubbles are significantly larger than the beads. When the bubbles and beads have comparable sizes, one-layer or two-layers 2D aggregates are generated due to the limited surface areas of the bubbles. Therefore, the formation mechanism of colloid has been revealed via numerical simulations.

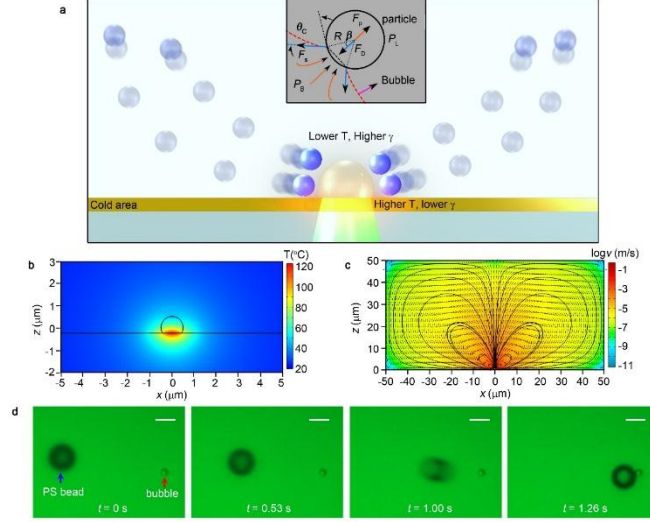


Figure 1: Particle trapping at a microbubble that is generated through the plasmon-enhanced photothermal effects. *a*, Schematic illustration of the particle-trapping mechanism by a single microbubble. The particles follow the convective flow due to the viscous force. The inset shows the force distributions when a particle is trapped by the microbubble (indicated as the red dash line). P_B and P_L indicate the pressure in the bubble and liquid, respectively, which introduce a net force of F_P pushing the particle outwards. The surface tension F_S introduce a drag force F_D . *b*, Simulated temperature distributions around a $1 \mu\text{m}$ bubble in a cross-sectional view. *c*, Simulated flow velocity distributions around a $1 \mu\text{m}$ bubble in a cross-sectional view. *d*, Time-resolved trapping process of a single $5.31 \mu\text{m}$ PS bead by a $1 \mu\text{m}$ bubble. Scale bar: $5 \mu\text{m}$.

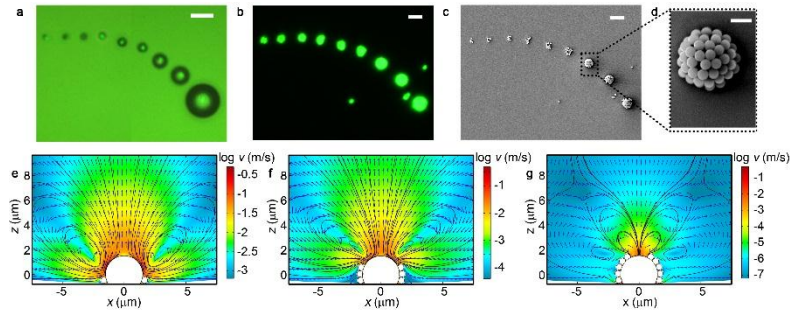


Figure 2: Patterning of the PS beads on the substrate at different laser powers. *a*, Optical micrographs of a series of microbubbles generated with the different laser power densities (0.64 – $1.12 \text{ mW}/\mu\text{m}^2$ from small to large bubbles). *b*, Dark-field optical micrographs and *c*, SEM image of the series of patterned 540 nm PS beads generated with corresponding power densities in *a*. *d*, High-magnification image of the 3D hollow. The flow velocity distributions (logarithmic scale) around a $3 \mu\text{m}$ microbubble in a cross-sectional view when *e*, single layer *f*, three layers and *g*, five layers of 540 nm PS beads are trapped at the gas/liquid interface. Scale bar: *a*–*c*, $5 \mu\text{m}$; *d*, $1 \mu\text{m}$.

Reference

1. T. Ito and S. Okazaki, *Nature*, 2000, **406**, 1027–31.
2. L. Lin, X. Peng, Z. Mao, W. Li, M. N. Yogeesh, B. B. Rajeeva, E. P. Perillo, A. K. Dunn, D. Akinwande, and Y. Zheng, *Nano Lett.*, 2015, **16**, 701–708.

Traction Force Threshold Signals Metastatic-Like Dispersion of Multicellular Epithelium

Yao Zhang and Sulin Zhang

Department of Engineering Science and Mechanics, The Pennsylvania State University,
University Park, PA 16802, USA

Cancer progression often accompanies with changes in tumor microenvironment. Examples include increased stiffness of extracellular matrix (ECM), altered ECM composition(1) and density of ECM proteins. Reciprocally, the altered microenvironment contributes to the progression of malignancy, in addition to the intrinsic genomic alternation of tumor cells. This complex interplay may arise from the dynamic and interwoven cell-microenvironment interactions. Indeed, tumor cells sense and process mechanical cues from their surroundings, and respond by activating biochemical signals, a process termed mechanotransduction. The biochemical signals in turn regulate cooperative remodeling of cytoskeleton, cell-cell adherens junctions, and cell-ECM focal adhesions, leading to altered cell motility and function. Despite of increasingly accumulated *in vitro* evidence of microenvironment-induced malignant phenotypes, the biochemical signals and molecular mechanisms triggering cancer metastasis and malignant transformation have not been identified.

Cell migration, particularly cancer metastasis, requires dynamic regulation of intracellular, intercellular, and extracellular forces(2). For individual cells, integrin-mediated focal adhesions pull ECM and sustain tension generated by actomyosin contraction(3). Coordinated pushing in the leading edge and retraction in the trailing edge lead to forward cell migration. In multicellular microtissues, intracellular contraction is transmitted to the cadherin-mediated adherens junctions as well as cell-ECM focal adhesions, generating long-range

tension inside the microtissues on the one hand, and traction force on the ECM on the other. The loss of the balance of these forces may result in dispersion of the microtissues into individual cells. Though it has been long hypothesized that tensional homeostasis is essential to cell morphogenesis, survival, and normal functions, much like the role of body temperature to human beings, how the mechanical force mediates and contributes to the progression of malignancy in tumors remains not fully understood.

Here we demonstrate through advanced traction force microscopy (TFM) that the traction force directs metastatic-like dispersion and malignant transformation of the human colon carcinoma (HCT-8) cell colonies upon prolonged culture time on polyacrylamide (PAA) gels. In particular, we reveal that a threshold of traction force exists below which the colonies remain cohesive and above which they disperse into individual malignant cells. Moreover, we quantify the intercellular tension through monolayer stress microscopy (MSM)(2). We demonstrate that intracellular contraction and intercellular tension are positively correlated with the extracellular traction, suggesting that all the cellular forces may serve as mechano-signals or mechano-markers for the onset of the metastatic-like dispersion and malignant transformation in the multicellular epithelium. Our results underscore the importance of the cellular forces for the onset of cancer metastasis and progression of malignancy.

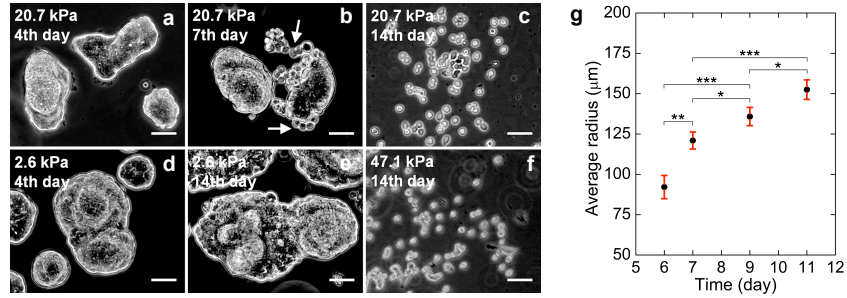


Fig. 2. Substrate-stiffness and colony size dependent dispersion of HCT-8 cell colonies. Scale bar: 50 μm . (a) At day 4 of culture on the 20.7 kPa gel, HCT-8 cells formed isolated cell colonies of different sizes and morphologies. (b) At day 7 of culture, cells at the periphery of one of the cell colonies dispersed from their mother colony, as indicated by the arrows. (c) At two weeks of culture, all the colonies dispersed into individual cells with a metastatic phenotype. (d-e) HCT-8 cell colonies on 2.6 kPa gels remained cohesive without dispersion throughout the culture period of two weeks. (f) HCT-8 cell colonies on 47.1 kPa gels exhibited similar dispersion behavior as seen on 20.7 kPa gels. (g) Dispersion kinetics is also colony size dependent. * $p < 0.05$; ** $p < 0.01$; *** $p < 0.001$ (unpaired two-tailed t -test). Error bars denote standard error of the mean.

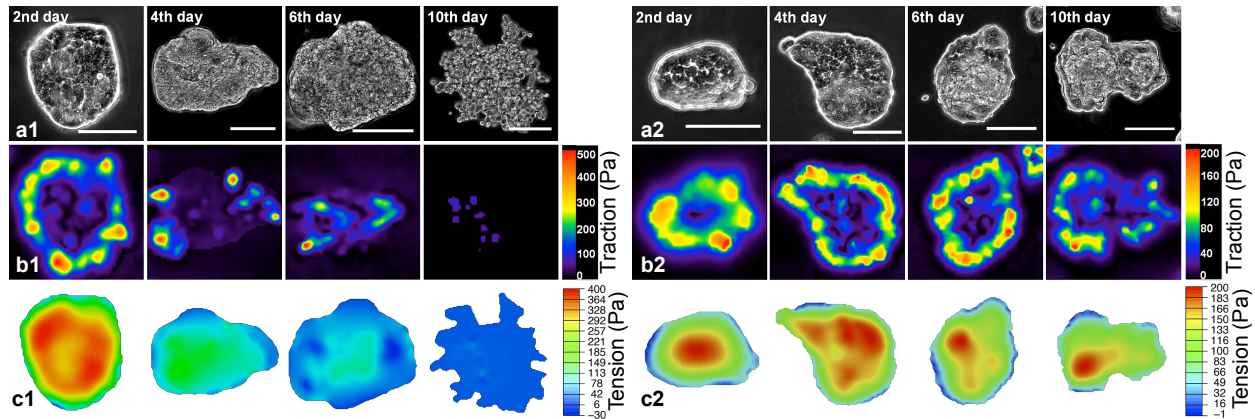


Fig. 3. Spatiotemporal traction and intercellular tension evolution of cell colonies cultured on 20.7 kPa (Left panel, a1-c1) and 2.6 kPa gels (Right panel, a2-c2). Scale bar: 100 μm . On 20.7 kPa gels, the traction force shifts from the periphery to the center from day 1 to day 6, and completely vanishes on day 10 (b1), underlying the dispersion of cell colonies. Such periphery-to-center shift of the traction force is absent in the cell colonies cultured on 2.6 kPa gels (b2). Correspondingly, the cell colonies cultured on 2.6 kPa gels maintains uniform tension inside the colonies (c2), while those on 20.7 kPa gels lose the tension as the dispersion progresses (c1).

Reference

1. Bergamaschi A, *et al.* (2008) Extracellular matrix signature identifies breast cancer subgroups with different clinical outcome. *J Pathol* 214(3):357-367.
2. Tambe DT, *et al.* (2011) Collective cell guidance by cooperative intercellular forces. *Nature Mater* 10(6):469-475.
3. Wang J-C & Lin J-S (2007) Cell traction force and measurement methods. *Biomech Model Mechanobiol* 6(6):361-371.

Actuating Capabilities of Laminates with F²MC tubes

Aniruddh Vashisth and Charles E. Bakis

Department of Engineering Science and Mechanics, Penn State, PA-16802, USA

Adaptive structures are mechanical structures which are capable of generating controllable response to the environment. As actuators, they can produce controllable force or shape change to modify the response of a system. Fluidic flexible matrix composite tubes (F²MC) tubes are fiber reinforced tubes with fibers embedded in an elastomeric matrix and could be categorized as adaptive structures. These tubes take inspiration from the fibrillar network found in plant cell walls which could behave like actuators and achieve large strains and blocked forces [1,2]. Research has been done to develop flexible matrix composite (F²MC) actuators which have the capability to achieve high degree of anisotropy by tailoring the fibers (orientation, number of layers, material, etc.) and selection of matrix materials [1,2]. Usually, these tubes are experimented with one end sealed and the other end fitted with a valve for controlling the fluid in and out of the tube. One can cause the actuator structure with F²MC tubes to contract, elongate (**Figure 1a**), or twist axially due to internal pressurization by designing the fiber orientation in the wall of the F²MC tube. It has also been shown that upon filling these tubes with fluid, the axial modulus could be increased many-folds. Mechanical model that could predict the characteristic properties of these tubes based on material property and orientation has been developed [3]. Recent investigation used tubes of diameters 3.2-20 mm. In an attempt to miniaturized adaptive structures with F²MC tubes, tubes with 2 mm diameter (**Figure 1b**) are used in this investigation.

The behavior of these millimeter sized F²MC tubes—individually as well as in unidirectional mono-layer laminate has been studied and experimentally characterized [4]. To exploit the capacity of these tubes to actuate, multi-layer laminates with F²MC tubes embedded are manufactured and

experimented. In this investigation, bilayer laminates were manufactured with two layers of unidirectional mono-layer laminate stacked one over the other. One of the layers of the laminate has contracting tubes, i.e. the tubes that contract upon pressurizing, whereas the other layer has extender tubes that extend upon pressurizing. Both the laminates are sealed at one end and are connected to a pressurizing channel at the other end so that both the laminates have the same internal pressure. Upon pressurizing the bilayer laminate, the F²MC tubes embedded in the laminate contract and extend creating a morphing structure (**Figure 2a**). By varying the arrangement of F²MC tubes in the bilayer laminate, a twisting or a warping [5] action could be produced. The behavior of the laminate could be tailored by selecting F²MC tubes with different fiber angle in each layer, modulus of the potting matrix, placement of the tubes in the laminate etc. Further a multi-layer laminate with F²MC tubes embedded in [60/0/-60]_S would behave quasi-isotropically in plane when either all the tubes are empty or filled with fluid. By closing and opening the valve for different layers of the multi-layered laminate, steerable stiffness could be achieved. Further, pressurizing different layers would result in morphing behavior in different direction.

The capabilities of these laminates to tune their shape and stiffness could be exploited by the aerospace industry to manufacture morphing wings. Bilayer laminates have displayed significant morphing abilities experimentally (**Figure 2a**). Single tube attached to cantilever beams has shown promise as vibration dampers by manipulating the fluid valve [6]. Multi-layer laminates with tubes embedded in multi-direction (**Figure 2b**) could be useful in controlling vibrational damping in different directions by controlling different valves.

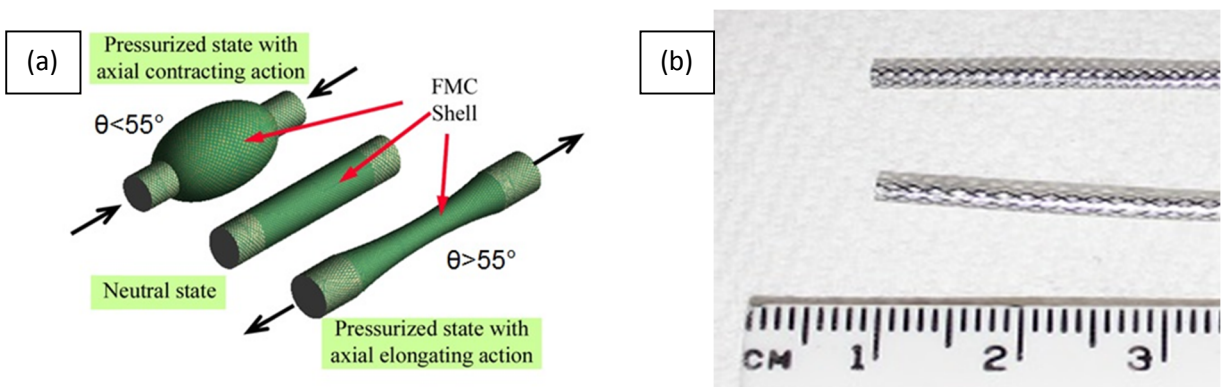


Figure 1. (a) Elongation or contraction of F²MC tubes upon pressurization. Fiber angle (θ) is the angle that the fiber makes with the axial direction. (b) F²MC tubes used in this investigation placed next to a centimeter scale.

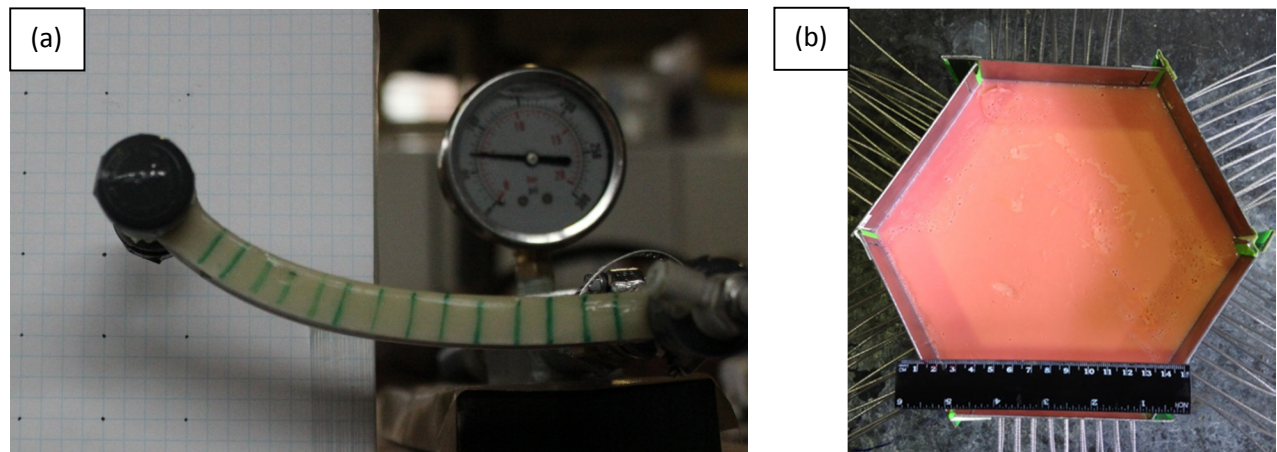


Figure 2. (a) Morphing upon pressurization in a bilayer laminate with contracting tubes in upper layer and extending tubes in the lower layer. (b) Multi-layer laminate with F²MC tube orientations [60/0/-60]_S with a capacity to steer stiffness and change shape long three different angles.

REFERENCES:

1. Philen, M., Shan, Y., Wang, K., Bakis, C., and Rahn, C.. Fluidic Flexible Matrix Composites for the Tailoring of Variable Stiffness Adaptive Structures. Proc. 48th AIAA/ASME/ASCE/AHS/ASC Structures, Structural Dynamics, and Materials Conf. Honolulu, HI, 2007.
2. Shan, Y., Philen, M., Lotfi, A., Li, S., Bakis, C., Rahn, C. and Wang, K.W. Variable Stiffness Structures Utilizing Fluidic Flexible Matrix Composites. Journal of Intelligent Material Systems and Structures, 20, pp. 443-456, 2009.
3. Zhu, B., Rahn, C. and Bakis, C. Actuation of fluidic flexible matrix composites in structural media. Journal of Intelligent Material Systems and Structures, 23(3) 269–278, 2012.
4. Vashisth, A., Zhu, B., Wimmer, B.M., Bakis, C.E. and Rahn C.D. Evaluation of Millimeter-Size Fluidic Flexible Matrix Composite Tubes. SMASIS2013-3344 Proceedings of the ASME 2013 Conference on Smart Materials, Adaptive Structures and Intelligent Systems, Snowbird, Utah, September 16-18, 2013.
5. Vashisth, A. [Aniruddh Vashisth]. Bilayer laminate with FMC tubes- Morphing behavior [Video file]. Retrieved from <https://www.youtube.com/watch?v=pbFiFvFHxRE>, July 4, 2014.
6. Zhu, B., Rahn, C. and Bakis, C. Design of a Fluidic Flexible Matrix Composite Damping Treatment for a Cantilever Beam. American Society of Composites-28th Technical Conference, State College, PA., 2013.

EXPERIMENTAL AND NUMERICAL INVESTIGATION OF SURFACE ACOUSTIC WAVE DRIVEN MICROPARTICLE ACOUSTOPHORESIS

Nitesh Nama, Tony Jun Huang, Francesco Costanzo

Department of Engineering Science and Mechanics, The Pennsylvania State University,
University Park - 16802, PA, USA

Surface Acoustic Wave (SAW) based systems have gained prominence in recent years for various lab-on-a-chip applications including particle and fluid manipulation. However, physical understanding of SAW devices is rather limited and so is the full understanding of the fundamental physical mechanisms, e.g. what is the mechanism behind the vertical focusing of particles in polydimethylsiloxane (PDMS) channels driven by SAW and what is the critical particle size for the transition between radiation-dominated and streaming-dominated acoustophoresis in these systems? In this work, we present a comprehensive numerical and experimental analysis of the acoustophoretic motion inside a PDMS microchannel actuated via SAW. Figure 1 shows a schematic of a typical device for SAW separation in a PDMS microchannel. We model the fluid using compressible Navier-Stokes equations without making any *a priori* assumptions about specific flow regimes. We employ a perturbation approach where the solution of the first-order equations is used to calculate the source terms in the time-averaged second-order equations, which are then solved to obtain the acoustic streaming field. Combining information from these two solutions, it is possible to estimate the mean trajectory of particles in the flow. Two forces govern the particle motion inside the flow: acoustic radiation force, F_{rad} , and the hydrodynamic drag force from the acoustic streaming. In most acoustofluidics problems the inertia of the bead can be neglected and thus, the velocity of the particles can be obtained using Newton's second law. We apply impedance boundary conditions to model the PDMS channel walls, while the bottom surface of the channel is subjected to a standing SAW. This actuation displacement is obtained via superposition of two SAWs traveling in opposite directions using the traveling SAW displacement

profile. The numerical solution was obtained via an in-house finite element code based on the *deal.II* finite element library. Figure 2 demonstrates the capability of SAW devices to precisely tune the position of the pressure node along the horizontal direction by tuning the phase difference between the two incoming traveling waves. Figure 3 shows the trajectories of polystyrene particles of diameter (b) 1 μm , (c) 5 μm , (d) 10 μm , (e) 15 μm , and (f) 20 μm . It can be seen that while the hydrodynamic drag force dominates the motion of the smaller particles, the motion of the large particles is radiation force driven and large particles are moved to the pressure node by the acoustic radiation force. We also validate these results with the experimental results relating to the 3D APTV measurements of time-evolving motion of 15 μm particles. Further investigations aiming at more comprehensive validation of our numerical model using 3D astigmatic particle tracking velocimetry (APTV) are ongoing. Such experimental verification would pave the road for further enhancements of our numerical model to include wall enhancement effects of the viscous drag force as well as the inclusion of the heat-transfer equation in the governing equations in order to account for temperature effects.

Acknowledgments: The experimental component of this work is being partially carried out in collaboration with Rune Barnkob, Institute of Fluid Mechanics and Aerodynamics, Bundeswehr University Munich, Germany.

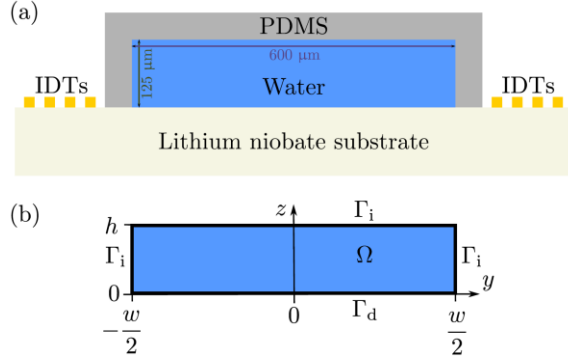


Figure 1: (a) Cross-sectional sketch of the SAW-driven device consisting of a lithium niobate substrate and liquid-filled PDMS channel (width $w = 600_{\mu\text{m}}$ and height $h = 125_{\mu\text{m}}$). The substrate is acoustically actuated via two sets of interdigitated electrodes (IDTs). (b) Sketch of the computational domain Ω with impedance boundaries and Dirichlet actuation boundary.

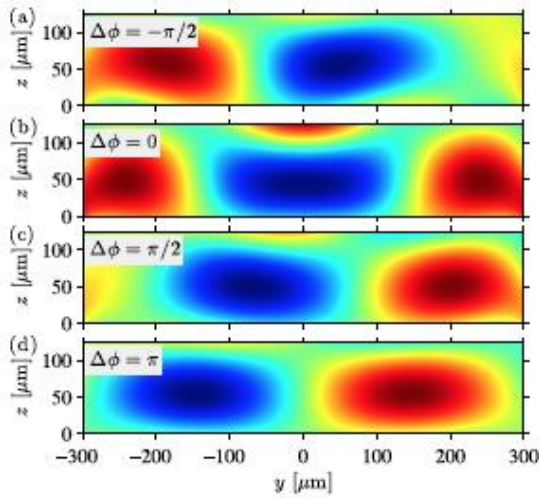


Figure 2: Color plots of the first-order pressure field for different values of phase difference between the two incoming traveling waves. The position of the pressure node along the horizontal direction can be tuned by changing the value of the phase difference such that the pressure node moves by a distance of $\lambda/8$ for each phase difference of $\pi/2$.

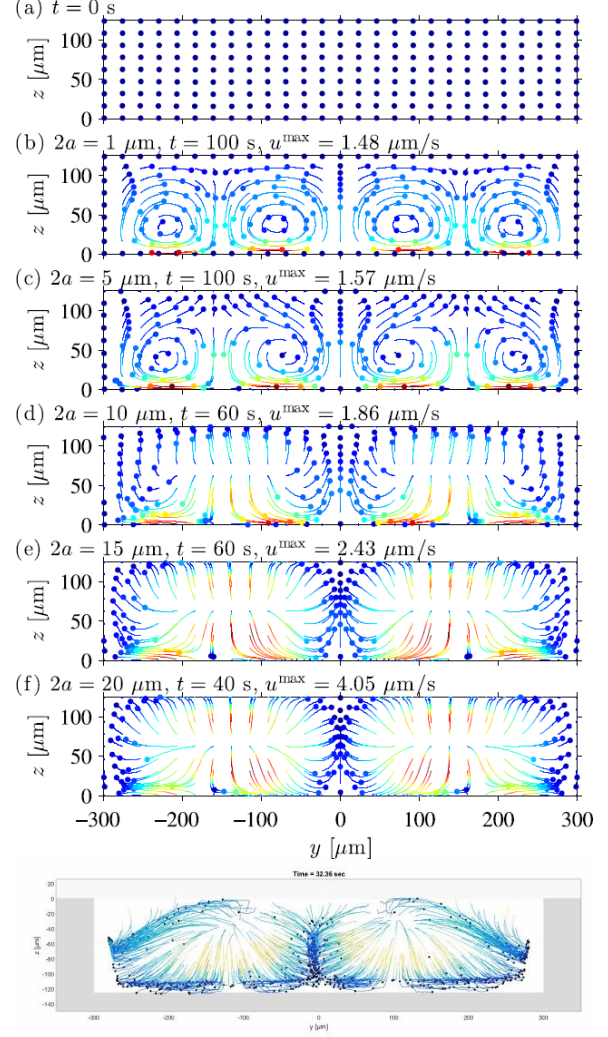
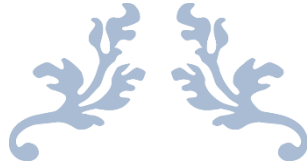


Figure 3: Comparison of experiments with 3D APTV measurements. (a-f) Particle trajectories with particle velocities as colors from blue minimum to red maximum and colored disks denoting the final positions within the observation time. (a) Starting position of 175 particles distributed uniformly within the microchannel. The panels (b)-(f) show the trajectories of (b) $1_{\mu\text{m}}$ particles during 100 s, (c) $5_{\mu\text{m}}$ particles during 100 s, (d) $10_{\mu\text{m}}$ particles during 60 s, (e) $15_{\mu\text{m}}$ particles during 60 s, and (f) $20_{\mu\text{m}}$ particles during 40 s. The motion of the smaller particles is dominated by the viscous drag force from the acoustic streaming, while the larger particles are pushed to the pressure nodes by the acoustic force. The last panel shows the experimental results relating to the 3D APTV measurements of time-evolving motion of $15_{\mu\text{m}}$ particles.



ESM TODAY 2016 POSTER ABSTRACTS

13th Annual Engineering Science and Mechanics Symposium



FEBRUARY 2, 2016
ENGINEERING SCIENCE AND MECHANICS (ESM) DEPARTMENT
THE PENNSYLVANIA STATE UNIVERSITY
212 EES BUILDING, SCE, PA 16803, USA

Erosion-Corrosion Behaviors of Multilayer Coating Systems for Internal Coating of Gas Pipelines

Dailin Wang

Department of Engineering Science and Mechanics, Penn State, PA-16802

The protection of gas pipelines in high-temperature, low-pH marine environments is of great importance. In addition to the detrimental corrosive action of seawater, the offshore infrastructure is subjected to sand erosion which itself can cause significant material degradation. Therefore, the main concern is the combination of erosion and corrosion since these two processes are often synergistic, leading to rapid failure. As a result, both corrosion and erosion should be considered during the integrity analysis of candidate coating systems for the internal protection of gas pipelines.

Erosion-Corrosion tests were carried out to evaluate the performance of two multilayer coating systems. One of the coatings was an organic coating system of powder phenolic novolac and liquid epoxy phenolic, with different coating thicknesses and amounts of filler. The other coating system was composed of a sacrificial layer (Organic and inorganic Zinc rich primer, Zn15Al,) underneath an organic coating layer (Polyurethane, Amine epoxy).

A custom-built controlled angle and velocity solid particle erosion tester was applied to impinge a set amount of Al_2O_3 particles on the coatings. The

coatings were immersed in a 60 degree centigrade solution of 2000 ppm $[\text{Cl}^-]$, pH 3.5, saturated with carbon dioxide, and removed to undergo erosion testing once a week. Electrochemical tests including open circuit potential (OCP) and Electrochemical Impedance Spectroscopy (EIS) were carried out to monitor the corrosion behavior of coating systems during immersion. The erosion-corrosion cycles were applied until penetration of the coating systems. The role of coating type, coating thickness, and the effect of amount of filler on the coating performance under erosion-corrosion were examined and evaluated.

A polymer-particle model was set up to evaluate the mechanical properties of the coating system under the impingement of erosive particles. Young's moduli and stress distributions for coating systems with different amounts of filler were calculated in the model and can be used to optimize the amount of filler in the coating systems. The relationship between erosion-induced micro cracks in the coating and corrosion resistance of the coating system has also been investigated.

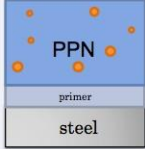
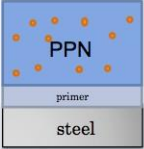
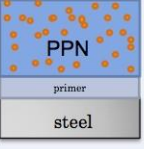
| Coating | Low filler | Standard filler | High Filler | Thickness |
|---------|---|---|--|---|
| PPN |  |  |  | Thin (All 4.5-6 mils) |
| PPN |  |  |  | Thick (Low f. 11-14 mils Std. f. 13-14 mils High f. 8-12 mils) |
| LEP | - |  | - | Thick 6.5-7 mils |

Figure 1. Organic coating system with different coating thicknesses and amount of filler (PPN: Powder phenolic novolac, LEP: Liquid epoxy phenolic)

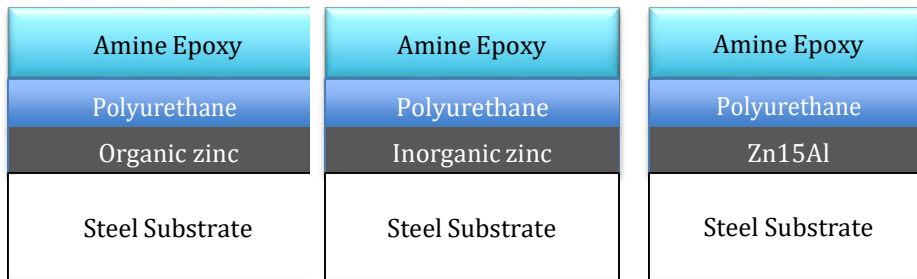


Figure 2. Coating system composed of sacrificial layer and organic topcoat

References:

Isin D. (2014). Development of new multifunctional coatings for protection against erosion and corrosion in Qatar oil and gas production (Master dissertation). Retrieved from <https://etda.libraries.psu.edu/paper/22761/>

Photocurable Dielectrics for Electronic Packaging and Encapsulant Application

W. Reainthippayasakul, Q. Wang, and M. Lanagan

Department of Engineering Science and Mechanics, Penn State, PA-16802, USA

In past decades, materials for electronic packaging and encapsulant applications have been paid considerable attention because of their promising functions in microelectronic devices and integrated circuit (IC) technology. Semiconductor encapsulation plays an important role to protect microelectronics from mechanical stress, electrical breakdown, chemical or moisture erosion, radiations, and so on. Among various kinds of materials, polymer-based encapsulants are highly recommended due to a balance between function, manufacturability, performance, reliability, and cost. In order to achieve high performance, a high dielectric strength (> 10 kV/mm) is required to prevent the breakdown in the package and a relatively high thermal conductivity (> 1 W/K-m) is also preferred to conduct the heat away from the components [1]. In addition, other factors including thermal stability, thermal coefficient expansion, mechanical strength, chemical and water resistance, ease of processing, and material cost would be considered.

Compared to conventional polymers, photocurable polymers provide some remarkable advantages including cure-on-demand properties, low energy consumption, possible solvent-free technology, high curing speed, and ambient temperature processing. Ultraviolet (UV) curing technology is one of the most effective techniques to transform multifunctional liquid monomer into crosslinked polymer networks, which is employed industrially in electronic packaging and encapsulant applications [2].

In the present study, various systems of UV-curable polymers and composites will be prepared and their related properties

such as thermal stability, thermal properties, dielectric properties, mechanical properties will be also investigated. In general, the thermosetting polymer films have been successfully fabricated by spin coating of mixed liquid monomer solution and then UV radiation. For example, thin films from the mixture of bisphenol A glycerolate diacrylate (BPAGDA) and trimethylolpropane triacrylate (TMPTA) with small amounts (3 wt.%) of photoinitiator 2-hydroxy-2-methylpropiophenone (HMPP) can be prepared and show good thermal stability over 400 °C. In addition, several thiol-ene polymer systems have been studied.

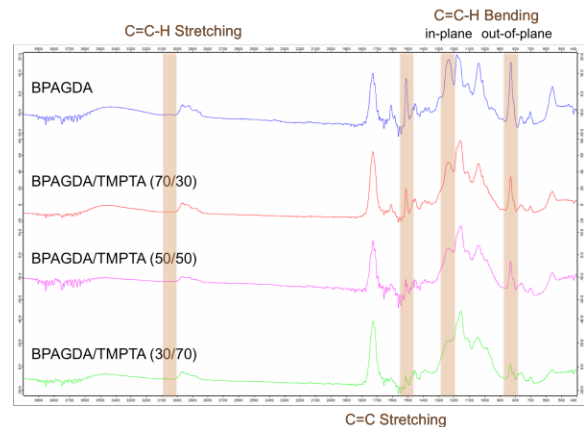


Figure 1: FTIR of thin films from the mixture of bisphenol A glycerolate diacrylate (BPAGDA) and trimethylolpropane triacrylate (TMPTA).

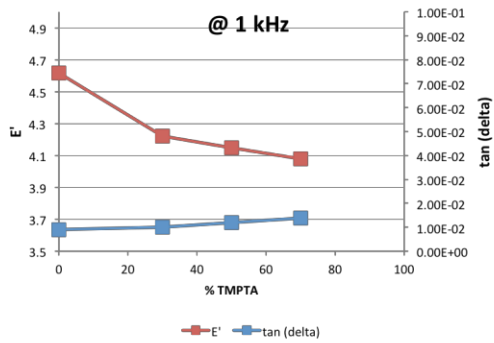


Figure 2: Dielectric permittivity and loss tangent of thin films from the mixture of bisphenol A glycerolate diacrylate (BPAGDA) and trimethylolpropane triacrylate (TMPTA) at 1 kHz and room temperature.

REFERENCES

- [1] Yao, Y.; Lu, G. Q.; Boroyevich, D.; Ngo, K. D. T. "Survey of high-Temperature Polymeric Encapsulants for Power Electronics Packaging" *IEEE Trans. Compon., Packag., Manuf. Technol.* **2015**, 5, 168-181.
- [2] Yu, B.; Wang, X.; Xing, W.; Yang, H.; Wang, X.; Song, L.; Hu, H.; Lo, S. "Enhanced Thermal and Mechanical Properties of Functionalized Graphene/thio-ene Systems by Photopolymerization Technology" *Chem. Eng. J.* **2013**, 228, 318-326.

When Mechanics Meets Electrochemistry: From Tiny to Mechanically Rechargeable Lithium Ion Batteries

P. Zhao and S. Zhang

Department of Engineering Science and Mechanics, Penn State, PA-16802, USA

The global energy challenge has motivated great efforts to the development of rechargeable batteries that are not only of high energy and high power, but also chemo-mechanically reliable. Lithium ion batteries (LIBs) is currently the best performing electrochemical energy storage technique. However, recent progress in chemomechanical modeling and in-situ transmission electron microscopy of the degradation mechanisms of a set of high-capacity electrode materials have shown that, LIBs with high-capacity electrodes (such as Si) suffer from rapid irreversible chemomechanical degradation and poor cyclability due to lithium insertion/extraction induced huge volume changes and subsequent fracture (Fig. 1).

Herein, in-situ transmission microscopy study and atomistically informed front-tracking modeling will be introduced to identify the electrochemically driven degradation mechanisms of nano-electrodes in lithium ion batteries (LIBs). From the vast differences in the in situ electrochemical cyclic behavior of silicon (Si) and germanium (Ge) we

highlight that lithiation kinetics and mechanical stress are strongly coupled: on the one hand lithiation kinetics modulates stress generation, defect nucleation and growth, and failure of the electrodes, and on the other, mechanical stress regulates the lithiation kinetics. Together, the stress-kinetics coupling determines the fate of the nanostructured electrode materials.

A set of in situ TEM experiments corroborated with chemomechanical modeling¹ (Fig. 2) are examined to support the coupled effects, spanning from anisotropic swelling in lithiated crystalline Si (c-Si)² versus isotropic swelling in c-Ge and amorphous Si (a-Si) that correspond to fragile behavior of c-Si and tough behavior of c-Ge upon lithiation, to stress-mediated lithiation retardation in c-Si and bending-induced symmetry-breaking of lithiation in Ge. Finally, implications of these studies on the design of durable lithium ion batteries are discussed. The findings offer fundamental guidance toward rational design of failure resistant high-performance LIBs.

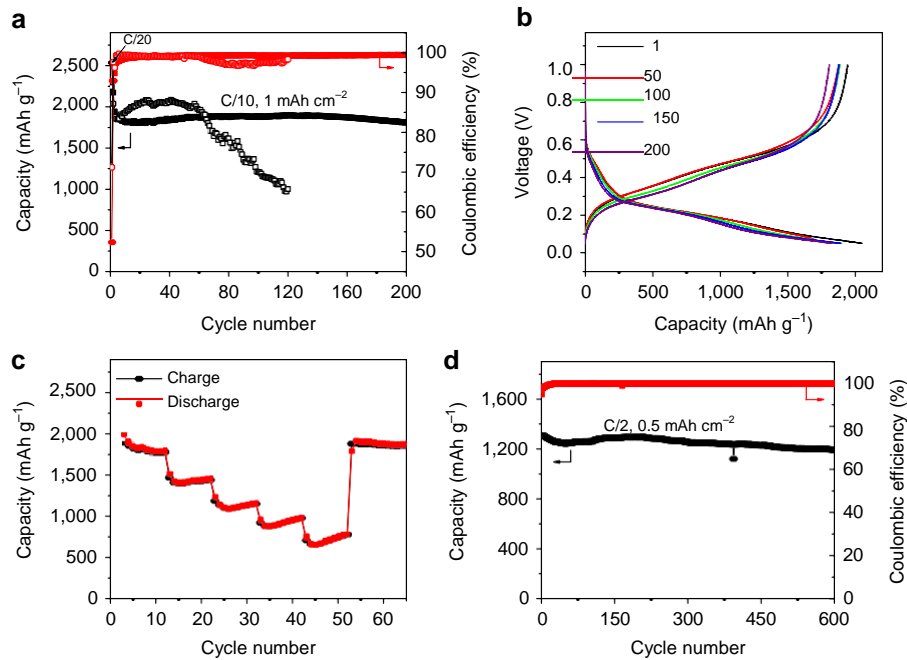


Figure 1. Electrochemical performance of the hp-SiNSs.

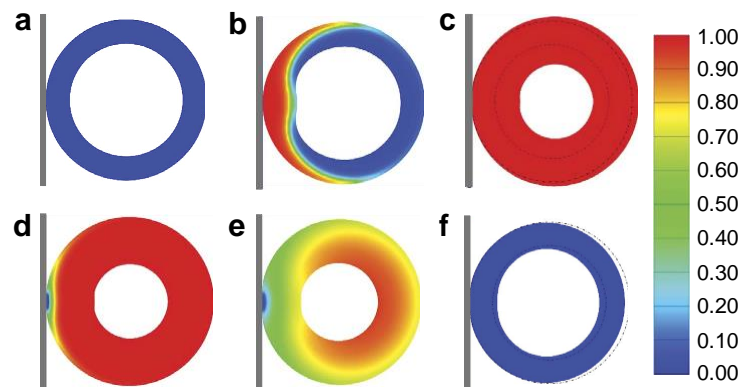


Figure 2. Chemomechanical modelling of the lithiation/delithiation processes of a hp-SiNS. Colours denote the Li concentration.³

REFERENCES

1. Yang, H., et al., *A chemo-mechanical model of lithiation in silicon*. Journal of the Mechanics and Physics of Solids, 2014. **70**: p. 349-361.
2. Yang, H., et al., *Orientation-dependent interfacial mobility governs the anisotropic swelling in lithiated silicon nanowires*. Nano letters, 2012. **12**(4): p. 1953-1958.
3. Xiao, Q., et al., *Inward lithium-ion breathing of hierarchically porous silicon anodes*. Nature communications, 2015. **6**.

Development of high energy density electrochemical capacitors for low power energy harvesting platforms

A. Aref, James Chou, R. Rajagopalan, M. Lanagan

Department of Engineering Science and Mechanics, Penn State, PA-16802, USA

Supercapacitors or ultracapacitors are receiving considerable attention due to their high power density, high energy density, as well as long cycle life. Therefore, they can be a good candidate to meet the energy and power demands for electric vehicle, renewable energy storage, smart grid and energy harvesting technologies [1]. Several types of electrochemical capacitors can be distinguished based on the charge storage mechanism. Electrical double layer capacitors (EDLC) store energy through double layer formation at electrode/electrolyte interface of high surface area electrodes, such as activated carbon, carbon nanotubes and graphene shown in Fig 1. A second group of electrochemical capacitors, known as pseudo-capacitors uses high rate charge transfer faradaic reactions for storing charge shown in Fig 2. As a result, high rate charge transfer faradaic reactions can aid in further boosting the capacitance of the electrode through pseudocapacitive interactions [2]. Several materials that include functionalized carbons, metal oxides and conducting polymers have been used to induce pseudocapacitance [3].

In addition, high surface area carbon materials with controlled porosity and

microstructure are excellent candidate for EDLC electrodes. For example, Polyfurfuryl alcohol is an excellent source to produce high purity microporous carbon materials. Upon pyrolysis, it produces a carbon with a very narrow pore size distribution and a mean pore size of ca. 0.5 nm. When activated by using carbon dioxide, it is possible to produce an ultra high purity carbon with less than 1–2 at% oxygen content and maintain a narrow pore size distribution, with a mean pore size of ca. 0.8 nm. This combination of high surface area and controlled porosity resulted in very promising capacitive performance Fig 3.

There is also considerable effort in improving the properties of electrolyte such that both the energy density and power density of the capacitors can be improved by providing high voltage electrochemical stability and faster ion transport [4]. Experimental techniques such as galvanostatic charge/discharge and impedance spectroscopy are the most common tools that are used to assess both the materials and device performance. In this work, the lithium ion capacitors made using high surface area nanoporous electrodes and a

prelithiated graphite anode are capable of energy density (300 J/cc) and demonstrate good self-discharge performance (90% charge retained over 3 months). The energy densities of these capacitors can be further improved by increasing the capacity of both the high surface area cathode and prelithiated anode. As part of our efforts, we are

synthesizing novel anode and cathode nanomaterials based on metal oxide/carbon nanocomposites that can potentially double the energy density. With the help of 3D current collectors, passivated electrode design and novel electrolytes, we also propose to design 4V EDLC with good leakage characteristics.

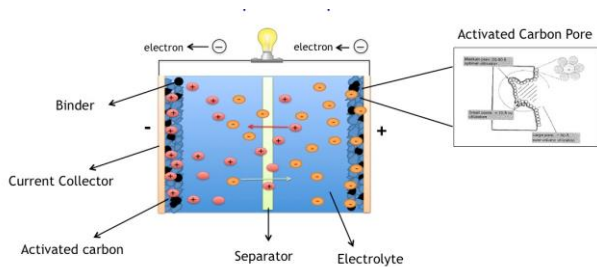


Figure 1: Electrochemical double layer capacitors(EDLC)

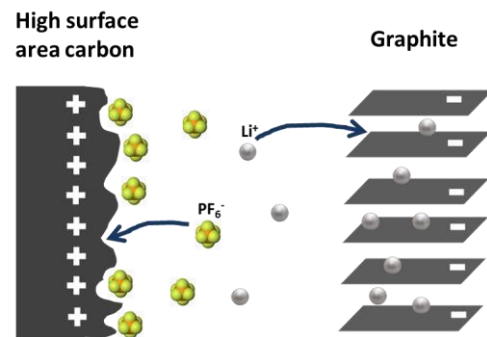


Figure 2: Lithium ion Capacitors

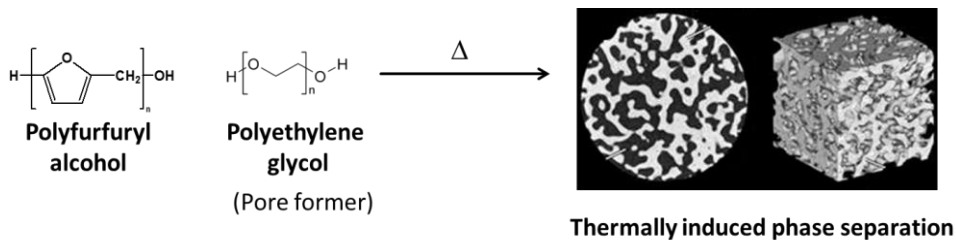


Figure 3: polyfurfuryl alcohol used as a precursor to make High surface area carbon with controlled porosity and microstructure

REFERENCES:

- [1] H. Budde-Meiwes, J. Drillkens, B. Lutz, J. Muennix, S. Rothgang, J. Kowal, D.U. Sauer, P I Mech Eng D-J Aut 227 (2013) 761.
- [2] J. Chen, C. Li, G.Q. Shi, J Phys Chem Lett 4 (2013) 1244.
- [3] V. Augustyn, P. Simon, B. Dunn, Energ Environ Sci 7 (2014) 1597.
- [4] F. Beguin, V. Presser, A. Balducci, E. Frackowiak, Adv Mater 26 (2014) 2219.

Local Temperature Field Sensing in Brain via Thin Film Vanadium Oxide Thermistor Arrays

M. W. Billard, H. A. Basantani, M. W. Horn and B. J. Gluckman
Department of Engineering Science and Mechanics, Penn State, PA-16802, USA

Temperature is fundamental indicator of normal or pathological neurological function in brain. Brain homeothermy is non-uniform and dynamic; temperatures vary within and between its different regions. These fluctuations in local and global temperature fields are driven by many regular factors that have associated changes in metabolic demand and perfusion. These factors include states of vigilance and changes in physical and mental activity. Abnormal neurological conditions or events, such as epileptic seizures, will disrupt temperature fields as well. High resolution characterization of temperature and heat transport on a scale relative to the size of local vasculature and functional cell groups could provide a direct insight into the effects of metabolic and perfusion changes on cells in real time. Overall, this could lead to understanding how brain temperature both modulates and is modulated by neural function in regular and pathological brain physiology.

Previous efforts to measure fine temperature fields in brain have been made, but with none meeting the full spectrum of criteria necessary for successful highly localized, real time temperature field recordings. An effective sensor for the previously mentioned applications would be minimally invasive, extremely sensitive, durable in the harsh ionic environment of cerebral spine fluid, and have sensors with a size and pitch scaled appropriately to the that of neural cells and capillary profiles. Primary issues with past probe designs included: low thermal or temporal resolutions; large device size; and high mechanical stiffness. These properties affect the devices ability to resolve the fine temperature gradients that may exist across cell groups or capillary beds, and may even impact the health of local biology to the point at which normal physiology is no longer discernible. The prototype flexible

neural probe presented here has been designed to meet all the criteria needed for a successful neural temperature sensor.

Eight regions of VOx were deposited with 150 μm pitch, as seen in Fig 1, onto glass and 20 μm polyimide substrates using Biased Ion Target Beam Deposition [1] [2] at the Penn State Materials Research Institute. Active VOx sensors were 10 μm \times 10 μm \times 85-nm-thick where 80 nm-thick top and bottom titanium leads, deposited using standard lithographic and sputtering techniques, intersected perpendicularly in the cross section. Polyimide samples were also passivated in parylene-C to protect the devices during chronic neural implantation. Prototypes on polyimide substrate are shown in Fig 2. Devices on glass were tested in vitro for thermal characteristics using a hot plate electrical probe station. Samples were continuously heated over a [20 57] $^{\circ}\text{C}$ range and current was measured in discrete 1mV steps through a [-10 10] mV range of actuation. Fig 3 shows the results of that experiment. Tested samples had an extracted mean thermistor temperature coefficient of resistance of $-4.060 \pm 0.004 \text{ \%}/^{\circ}\text{C}$. Nominal room temperature resistance for the thermistors was approximately 1.3 MW [3].

Continued research will be conducted over the next year which will include additional fabrication and further in-vitro testing, as well as in-vivo experimentation. Arrays will be tested on a PID-controlled temperature bridge to assess ability to resolve fine thermal gradients on a scale similar to what is likely to be seen in across neuron groups and capillary beds in brain. The final goal is application of the probes in in-vivo chronic measurement of localized temperature field dynamics of specific brain regions in normal and epileptic animals.

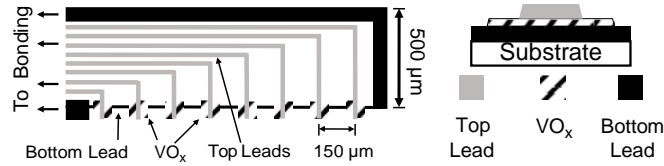


Figure 1: Diagram of the array layout from top (left) and cross-sectional view of thermistor design (right). VO_x (hashed) is deposited between perpendicular leads to make $100 \mu\text{m}^2$ thermistors.

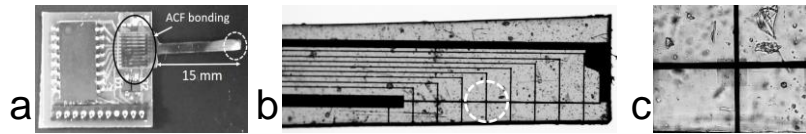


Figure 2: **(a)** A full neural probe with actuation circuitry. The shank length is 15 mm. Micrographs of **(b)** a thermistor array and **(c)** an individual sensor. The dark traces are the top and bottom leads of the device. For scale, these traces are $10 \mu\text{m}$ wide. The light square where the traces cross is the VO_x deposit. This device has been coated with an appropriately $3\text{-}5 \mu\text{m}$ thick layer of parylene-C to protect the sensors. The passivation accounts for textural irregularities seen in both **(b)** and **(c)**.

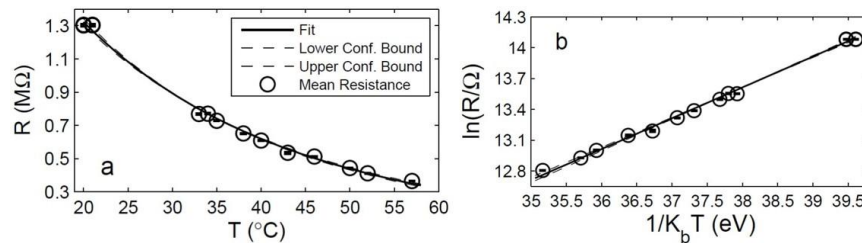


Figure 3: **(a)** Resistance vs temperature relationship of the thermistors. **(b)** Log of sample resistance vs the inverse of $K_b T$. The negative of the slope is the activation energy of the thermistor, $-0.3003 \text{ eV} \pm 0.004$. A TCR of $-4.060 \pm 0.004 \text{ \%}/^{\circ}\text{C}$ was derived using using an Arrhenius relationship at a temperature of $20 \text{ }^{\circ}\text{C}$. Error bars indicate a propagated uncertainty from both the mean resistance measurements and the data fitting.

References

- [1] Y. Jin, H. A. Basantani, A. Ozcelik, T. N. Jackson, and M. W. Horn, "High-resistivity and high-TCR vanadium oxide thin films for infrared imaging prepared by bias target ion-beam deposition," *Proc. SPIE 8704 Infrared Technology and Applications XXXIX*, vol. 87043C, 2013.
- [2] H. A. Basantani, *Thin Film Materials and Devices for Resistive Temperature Sensing Applications*. Phd dissertation, engineering science and mechanics, The Pennsylvania State University, 2014.
- [3] M. W. Billard, H. A. Basantani, M. W. Horn, and B. J. Gluckman, "A Flexible Vanadium Oxide Thermistor Array for Localized Temperature Field Measurements in Brain," *Sensors Journal, IEEE*, vol. PP, no. 99, pp. 9–10, 2016.

MULTIFUNCTIONALITY OF PARYLENE C MICROFIBROUS THIN FILMS

Chandraprakash Chindam, Osama O. Awadelkarim, and Akhlesh Lakhtakia
Department of Engineering Science and Mechanics, Penn State, PA-16802, USA

Engineering often involves designing products that accomplish one specific function. A glimpse into nature can make us think that a design can serve more than one function. For example, leaves of plants are designed to transport nutrients across the neighboring cells, release carbon dioxide, and also absorb sunlight. Some leaves, for e.g. lotus leaves, are also capable of self-cleaning. The skin of animals including humans serves multiple functions such as holding the muscles and body parts in place and shape, facilitate sweating and holding hair follicle for maintaining body temperature, and maintain the sense of touch. While multifunctional instruments remain rare in engineering, some current day products such as a printer serve many functions: copy, scan, print, email, and fax. Although some multifunctionality is achieved here, it is a conglomeration of many single-function devices. For a sustainable future, we need to decrease the number of single-function devices, create multifunctional devices and make them as smaller as possible. Moreover, in current age of miniaturization, the size of sensors and devices is shrinking rapidly and most of the fabrication is by achieved via thin film deposition. In the quest for a multifunctional sensor, here, we make use of existing procedures in thin film fabrication and explore it for different applications. Also to enhance the number of functions, we start with a material that already has industrial applications and is explored in research circles.

Parylene C, a chlorinated member of the xylylene polymer family, has been extensively used as a packaging material in industry [1] – electrical insulation coatings in electronics and corrosion-resistant coatings over prosthetic parts. On the research front, it has been used to study biological cells for retinal prosthesis, and cancer studies.

We earlier explored this material for the growth of human fibroblast cells and also modified the industrial physicochemical vapor deposition technique [2] to fabricate inhomogeneous thin films with periodicity in their microstructure. We call these films as microfibrillar thin films (μ TF) of Parylene-C polymer. These μ TFs comprise parallel arrangement of periodically spaced microfibers of shapes circular-cylindrical, chevronic, and chiral [3] with their diameter ranging between 3.3 and 5 microns. Using these μ TF, the objective is two-fold. First, we computationally investigate these μ TF as Phononic and Photonic crystals. Next, we fabricate μ TF and determine their frequency- and temperature-

dependent mechanical and dielectric properties, aiming them for sensors.

For both photonic and phononic band gap calculations, the microfibers are considered to be arranged as hexagonal and cubic lattices and host mediums are air and water. Eigenfrequencies were determined for all paths in the irreducible Brillouin zones of hexagonal and cubic lattices. We note that the chevronic and chiral μ TFs are periodic in three dimensions and the cylindrical μ TF is periodic in two dimension. After validating the 2-D solid-inclusion-in-fluid-host model and a 3-D solid-inclusion-in-solid-host model developed in COMSOL with Matlab, the elastodynamic eigenfrequencies of all the chiral, chevronic, and cylindrical μ TF embedded in air and water are determined and bandgaps were identified from the dispersion plots. To determine the photonic bandgaps MPB, scheme-language-based open-source programming software, was used. Validation of these MPB programs was made using on established cases and Matlab. Prior to determining the photonic bandgaps, the dielectric properties of Parylene-C polymer were determined using a combination of infrared transmission experiment and genetic algorithm. We found that all three morphologies of μ TF have at least one bandgap in both hexagonal and cubic lattice, regardless of the host medium. Since the elastic properties of Parylene C are closer to those of water, more elastodynamic bandgaps exist for those cases where air is host medium. The phononic and photonic bandgaps lie in the 1-100-MHz and infrared regimes, respectively.

Cylindrical μ TF films and bulk films were deposited and subjected to cyclic elastic loading testing in a Dynamic Mechanical Analyzer from -40 °C to 125 °C and frequencies from 1 to 80 Hz. We found that the μ TF films are at least ten times lower in storage and loss modulus compared to the homogeneous bulk film. The relative lower moduli suggests their compliant nature and a higher glass transition temperature of the μ TF indicates their use over a wider temperature range than the bulk film. Dielectric measurements performed in similar temperature range and frequencies 100 Hz to 1 MHz, revealed that the μ TF have a higher dielectric permittivity than the bulk film suggesting their use as charge storage materials. In conclusion, we have proved that these μ TF of Parylene-C can be used as anisotropic band filter in acoustics, infrared filter, charge-storage material and also as a soft material. capable of sensing based on mechanical properties.

REFERENCES

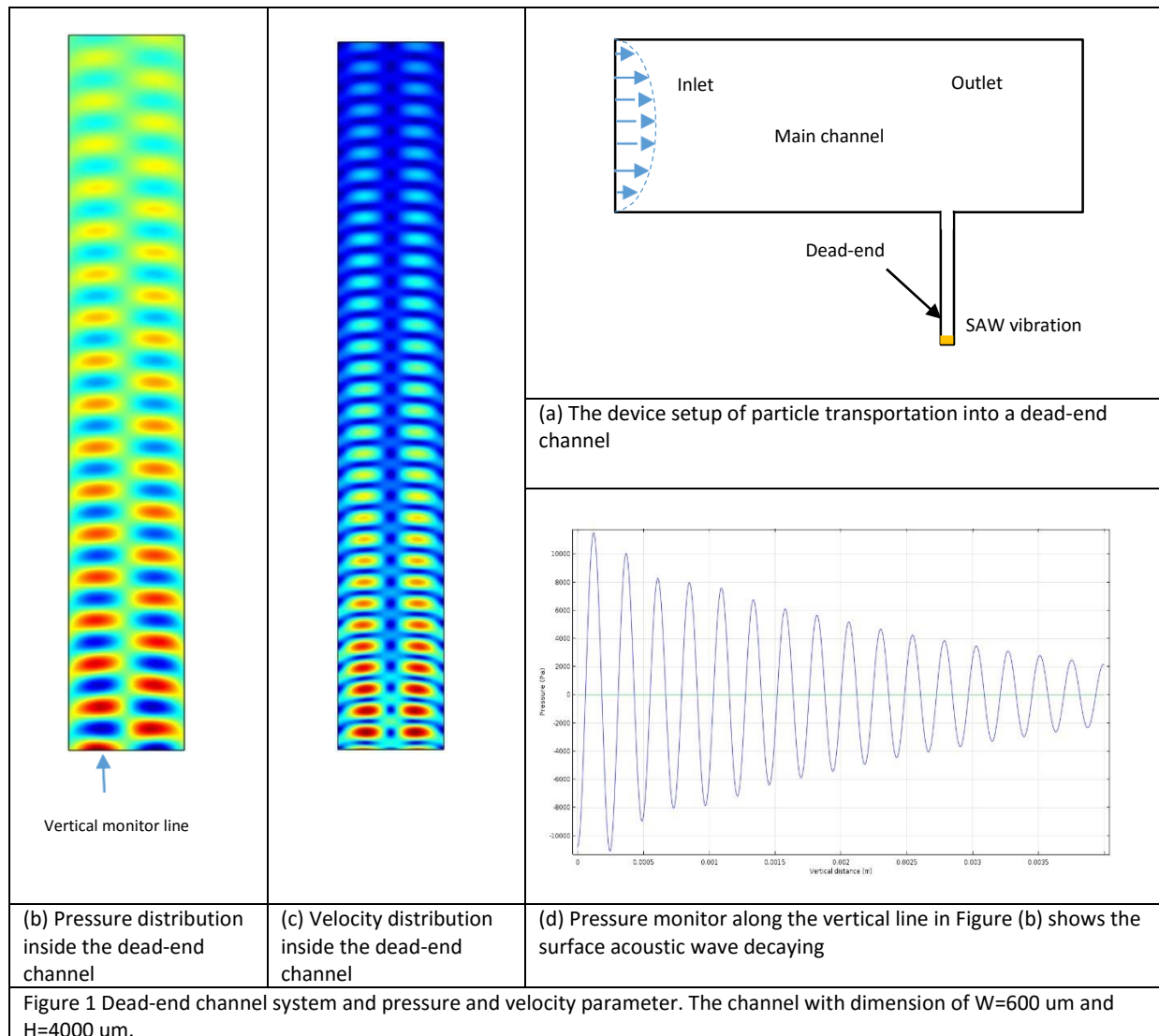
- [1] J. B. Fortin, T.-M. Lu, *Chemical Vapor Deposition Polymerization: The Growth and Properties of Parylene Thin Films*, Kluwer Academic, 2004
- [2] S. Pursel, M. W. Horn, M. C. Demirel, and A. Lakhtakia, "Growth of sculptured polymer submicron wire assemblies by vapor deposition," *Polymer.*, **46**, pp. 9544-9548, 2005.
- [3] C. Chindam, N. M. Wonderling, A. Lakhtakia, O. O. Awadelkarim, W. Orfali, "Microfiber inclination, crystallinity, and water wettability of microfibrinous thin-film substrates of Parylene C in relation to the direction of the monomer vapor during fabrication," *Applied Surface Science*, **345** pp 145-155, 2015.

Acoustic wave enhanced particle transportation in dead-end channel

Zhifeng Zhang, Niitesh Nama, Francesco Costanzo and Tony Jun Huang

Engineering Science and Mechanics, Penn State University, State College, PA, 16802

The dead-end channel is defined as the fluid channel with the outlet blocked, thus there are nearly no fluid going in and going out. This kind of dead-end channels at micro- and nanoscale are ubiquitous in nature and engineering problems such as the biological system like the extracellular matrix in the brain or the engineering problem like drug delivery. One of the difficulty in microfluidic is the particle and fluid transportation into this kind of dead-end channel. The reason for the difficulty is that there is no net fluid flow or mass flows into the channel by commonly used pressure driven flow control. As known, the Brownian movement is nearly the only mechanism of particle and fluid transportation. But the transportation efficiency is extremely low.



Besides the Brownian movement, recent research used chemical gradient [1] and solute concentration difference [2] to force the particle into the dead-end channel. Another potential method for the mass transfer is to use an active method like the acoustic wave. In this research, we used the travelling acoustic wave source to stimulate the mass transfer from the main channel to the dead-end channel. The pressure and velocity parameter are obtained from numerical simulation. In this method, the vibration source at the bottom of the channel can generate positive and negative pressure node at the same time. Thus the energy or in the form of acoustic streaming can take the fluid and particle from the bottom of the channel to the top of channel. At the same time, they bring the particle back to the bottom, thus form a circulation.

Reference

- [1] A. Kar, *Self-generated diffusiophoresis in dead-end pores*, THE PENNSYLVANIA STATE UNIVERSITY, 2015.
- [2] S. Shin, E. Um, B. Sabass, J. T. Ault, M. Rahimi, P. B. Warren and H. A. Stone, *Proceedings of the National Academy of Sciences*, 2016, **113**, 257-261.

ACOUSTIC ISOLATION OF WHOLE BLOOD EXTRACELLULAR VESICLES

Rui Zhang and Tony Jun Huang

Department of Engineering Science and Mechanics, The Pennsylvania State University, PA, 16802, USA

Blood transfusion is a common and crucial part in modern health service. Monitoring the safety of blood products is necessarily required. In the past few years, extracellular vesicles (EVs) were noticed as valuable biomarkers for diagnostics and therapeutics. In stored blood, the number of secreted EVs has been observed to increase over time, suggesting their potential as the metric for blood aging. However, the small size (<200 nm) of EVs and their complex biological environment raise a significant technical challenge in sample preparation. Long isolation time, large sample volume, and expensive reagents are usually needed, limiting the rapid and convenient analysis of EVs [1]. The acoustic tweezers technique has been developed to separate different bioparticles based on small differences in their size, density, and compressibility [2]. We herein report a tilted angle standing surface acoustic wave (taSSAW) based isolation system that size-specifically separates EVs from whole blood in a label-free and contact-free manner.

Figure 1 showed the schematic of the taSSAW based EV separation device. A pair of parallel interdigital transducers (IDTs) was deposited on the lithium niobate (LiNbO_3) substrate. A PDMS microchannel was bonded to the piezoelectric substrate with an inclined angle of 5° to the IDTs. When a power signal is applied to the IDTs, surface acoustic waves are generated, which propagate toward each other and leak into the flowing whole blood inside the channel. The interference between the IDTs forms an acoustic field and generates parallel pressure nodes and antinodes. Bioparticles are pushed toward the pressure nodes. Due to the size difference, red blood cells (RBCs) experience a larger acoustic radiation force than EVs. As a result, RBCs have a larger vertical displacement than EVs.

Whole blood sample and 1xPBS sheath flows were injected to the microfluidic channel through three

separated inlets. When the taSSAW field was OFF, the whole blood sample flowed into the top outlet as shown in Fig. 2a. Once the taSSAW field was ON, blood cells, as shown in Fig. 2b, were separated from the whole blood sample stream and flowed into the bottom outlet. Meanwhile, EVs remained in the sample stream and then flowed into the top outlet, thereby isolating EVs from the whole blood sample. Following the EVs isolation experiments, both the samples collected from two outlets were measured by dynamic light scattering. Figure 2c and 2d showed the analysis of size distribution for the samples collected at the top and bottom outlet, confirming the taSSAW separation device was effective for the isolation of EVs from whole blood.

Finally, the changes of EVs counts were monitored with whole blood of different storage days. 50 μL whole blood units at different time points were processed on our taSSAW separation device with the same acoustic separation parameters. Isolated EVs were collected from the top outlet after taSSAW separation and measured by nanoparticle tracking analysis (NTA) with the same setting. Figure 3 showed the significant increasing of whole blood EVs over storage time.

In conclusion, we demonstrated a taSSAW based continuous flow isolation approach of whole blood EVs. Compared to conventional EVs isolation methods, the taSSAW separation system is label-free, fast, inexpensive, and gentle on vesicles, making the acoustic EVs separation system as a reliable tool for EV related study. The taSSAW system can also be used as a standard of blood aging, holding great potential in blood product quality monitoring.

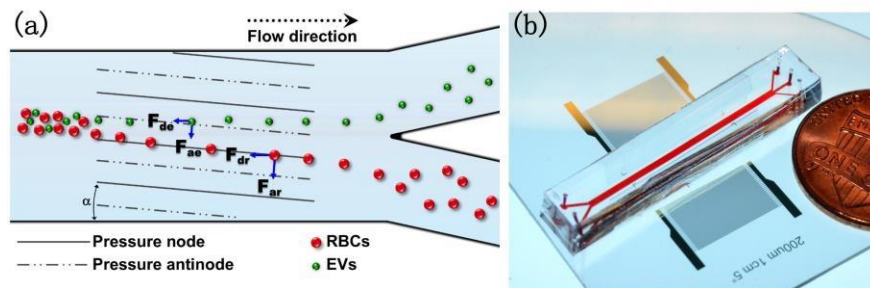


Figure 1: (a) The working mechanism of the taSSAW based EV separation. The direction of the pressure nodes and pressure antinodes were established at an angle of inclination (α) to the fluid flow direction inside a microfluidic channel. RBCs experience a larger acoustic radiation force (F_{ar}) than EVs (F_{ae}). F_{dr} and F_{de} are the drag force experienced by RBCs and EVs, respectively. (b) The fabricated taSSAW separation device with a penny for comparison.

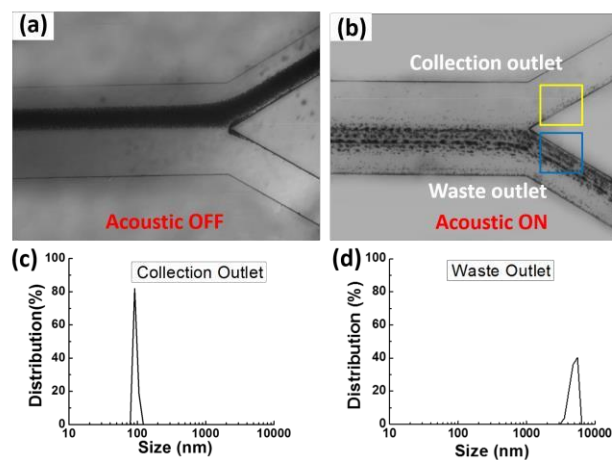


Figure 2: Isolation of EVs from whole blood. The collection and waste outlets when acoustic off (a) and on (b). The size distribution of collected samples were measured by dynamic light scattering (c) and (d).

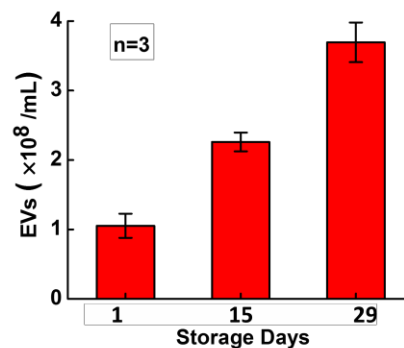


Figure 3: Monitoring the EVs concentration change in stored whole blood. EVs from whole blood units at different storage time points were isolated with the taSSAW separation device and measured with NTA, indicating the significant increasing of EVs over time.

REFERENCES

- [1] K. Lee, H. Shao, R. Weissleder, and H. Lee, *ACS Nano*, 2015, **9**, 2321-2327.
- [2] X. Ding, Z. Peng, S. Lin, M. Geri, S. Li, P. Li, Y. Chen, M. Dao, S. Suresh, and T. J. Huang, *Proc. Natl. Acad. Sci. U. S. A.*, 2014, **111**, 12992-12997.

Improved Traction Force Microscopy For Cell Mechanics Studies

Qiong Wei and Sulin Zhang

Department of Engineering Science and Mechanics, Penn State, PA 16802, USA

Recent evidence has shown that the establishment of cell traction force by transmitting acto-myosin contractility onto extracellular matrix (ECM) *via* integrin-dependent focal adhesions (FAs) is crucial for regulating cell behaviors and functions, such as adhesion, proliferation, migration and differentiation. Thus, a quantitative tool for measuring cell traction force is essential for studying the way cells sense and response to their mechanical micro-environment.

The prototype of traction force microscopy (TFM) was developed by Harris and his co-workers. By applying known forces to suppress the wrinkling of the thin silicone rubber film induced by cells, Harris *et al.* were able to semi-quantitatively assess the magnitude of cell traction force^[1]. However, the inherent non-linearity of the silicone rubber deformation and low spatial resolution of wrinkling assessment greatly limit this approach. Further development of tools for quantitatively mapping traction force has burst over the last 30 years. A widely used tool is micro-pillar assay method^[2], in which an array of micro-fabricated pillars serves as the force sensor and the cell traction force could be derived at each point from the pillar's deflection by using Euler-Bernoulli beam theory. Micro-pillar assay is a discrete method for readout of traction force, but not a best choice for cases that cell adhesions are not spatially confined.

Alternatively, a continuous TFM method has become a standard choice to reconstruct the cell traction force^[3]. The principle is illustrated in Fig. 1. As a cell adheres to a complaint flat elastic substrate labeled with fluorescent markers, it will deform the

substrate. The deformation is tracked by capturing the lateral movement of fluorescent markers embedded in the substrate through a comparison of the deformation image in which the substrate is deformed by cell traction force and the reference image in which the deformation is removed due to enzymatic detachment of the adherent cell. By solving an inverse elasticity problem based on the displacement field together with the assumption of elastic infinite half-space plane, the mapping of traction force beneath the adherent cell can be derived. Fluorescent markers, served as the tracer of substrate deformation, play a key role in estimating cell traction force. Ideally, the markers should be on the same plane beneath the top surface of the substrate with a proper density. In tradition, researchers mix fluorescent beads uniformly into the pre-polymerization solution and roughly set beads on the surface of the substrate by quickly reversing the sandwich-like structure before polymerization of the hydrogel happens (Fig. 2b)^[4]. Errors in displacement field resulted from the background noise of fluorescent beads could be further amplified into the resulting traction force, which significantly limits the resolution of TFM. To reduce the background noise, we adopt a method published by Knoll *et al.*^[5] with some modification to localize fluorescent beads on the same plane that is 200nm beneath the substrate surface (Fig. 2a). *Via* the improved traction force microscopy, we successfully capture the traction force of several different cell types, including single cancer cell, *in vitro* microtumors and the contractility change of differentiated cardiac cells within a beating cycle (Fig. 3).

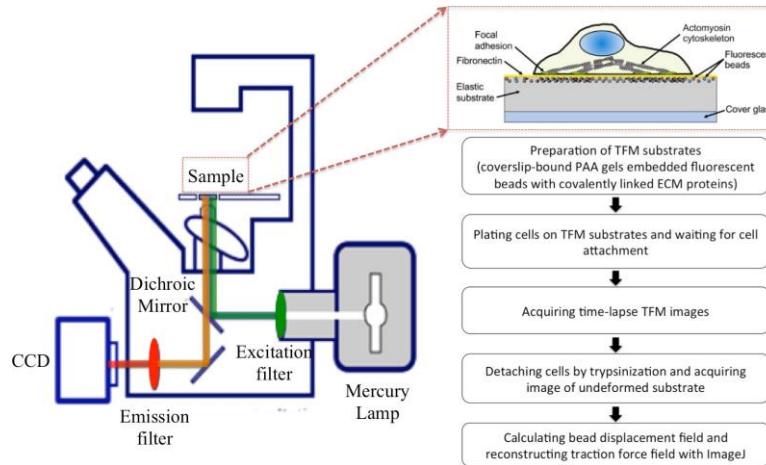


Fig. 1 The schematic of traction force measurement.

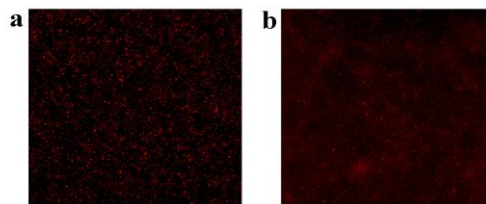


Fig. 2 Comparison between fluorescent beads embedded in PAA hydrogel with different method. (a) Improved method. (b) Traditional method^[4].

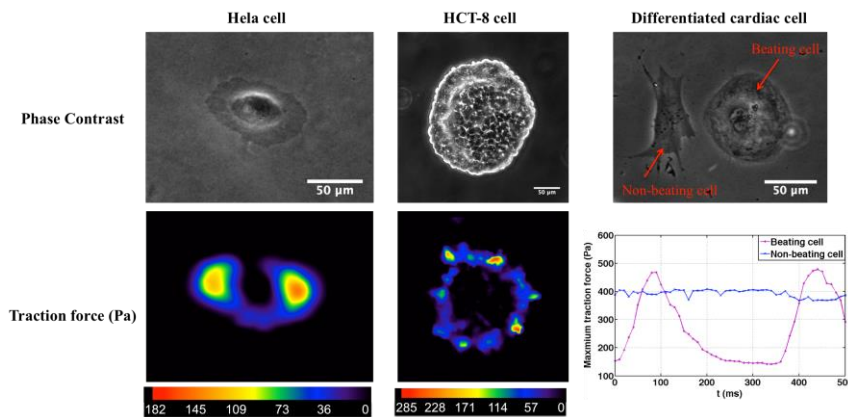


Fig. 3 Traction force measurement of different cell types on PAA hydrogel. (a) Single cancer cell (Hela). (b) In vitro microtumor (HCT-8). (c) Contractility change of differentiated cardiac cells within a beating cycle.

Reference

- [1] A.K. Harris, P. Wild, D. Stopak, Silicone rubber substrata: a new wrinkle in the study of cell locomotion. *Science* 1980, 208(4440), 177-179.
- [2] J.L. Tan, J. Tien, D.M. Pirone, D.S. Gray, K. Bhadriraju, C.S. Chen, Cells lying on a bed of microneedles: an approach to isolate mechanical force. *PNAS* 2003, 100 (4), 1484-1489.
- [3] S.V. Plotnikov, B. Sabass, U.S. Schwarz, C.M. Waterman, High-resolution traction force microscopy. *Methods in cell biology* 2014, 123, 367-394.
- [4] J.L. Martiel, A. Leal, L. Kurzawa, M. Balland, I. Wang, T. Vignaud, Q. Tseng, M. Théry, Measurement of cell traction forces with ImageJ. *Methods in cell biology* 2015, 125, 269-287.
- [5] S.G. Knoll, M.Y. Ali, M.T.A. Saif, A Novel Method for Localizing Reporter Fluorescent Beads Near the Cell Culture Surface for Traction Force Microscopy. *JoVE* 2014, (91), e51873.

Electrochemical Impedance Spectroscopy (EIS)-based Corrosion Sensor

F. Kim

Department of Engineering Science and Mechanics, Penn State, PA-16802, USA

Coatings are the first line of defense against corrosion on metals, such as the coated metal surfaces underneath the well-planking of Navy amphibious ships, but these coatings degrade over time and require maintenance. Currently, a schedule-based maintenance system, in which the coatings are removed periodically and reapplied without any knowledge of the coating condition, is employed. Not only does this waste time and resources, it reduces the ship's availability to the Navy. A sensor that monitors coating degradation would allow for a transition to a condition-based maintenance system in which maintenance is performed when the coatings have failed. Additionally, a sensor would enable corrosion detection in hard-to-access areas. A three-electrode electrochemical impedance spectroscopy (EIS)-based sensor was fabricated by screen-printing commercially available conductive inks onto a polymer top-coated polyimide substrate. Silver/silver chloride (Ag/AgCl) and graphite inks were evaluated as reference and counter electrode materials. A photograph of the sensor can be seen in Figure 1. Sensor performance was tested under the GM9540P/B cyclic corrosion testing protocol, modified with full-strength artificial seawater, in a salt spray cabinet. This protocol was chosen because the alternating cycles of mist, dry, humidity, and elevated temperatures (maximum temperature of 60°C) best represent the corrosive conditions seen in the tailgate area of Naval amphibious ships. Electrochemical Impedance Spectroscopy was run with a

frequency sweep of 100000 Hz to 0.01 Hz, 7 points per decade, and 10 mV AC Voltage. EIS results collected with the sensor were compared to EIS results (same coatings and same exposure conditions) collected with a commercial cell. The setup with the commercial cell can be seen in Figure 2. The sensor results closely followed the same trend of the control results.

The sensor was found to perform well in an aggressive environment in the salt spray cabinet for up to 165 days as the sensor data follows the same trend as the control data. To date, 165 days is the longest exposure time that has been evaluated for this sensor. An intentional pinhole coating defect was created at the edge of a test panel away from the sensor. The sensor detected a different trend in the EIS data after the defect was created thereby demonstrating its ability to detect a defect. The EIS Bode plot obtained from this experiment can be seen in Figure 2.

As Ag/AgCl degrades under UV exposure, determining sensor sensitivity to UV is explored in current research for possible aerospace applications. The sensor on coated relevant aluminum panels was exposed to a salt mist for two weeks and then UV exposure for two weeks. The sensor is performing well as data obtained from this sensor followed the same trend as the data obtained from the control. The sensor has not yet been evaluated in the colder temperatures for aerospace applications. To date, four weeks is the longest exposure time that has been evaluated for this sensor.



Figure 1: The photograph of the electrochemical impedance (EIS)-based sensor with screen-printed Ag/AgCl counter and reference electrodes adhered to a coated Army test panel.

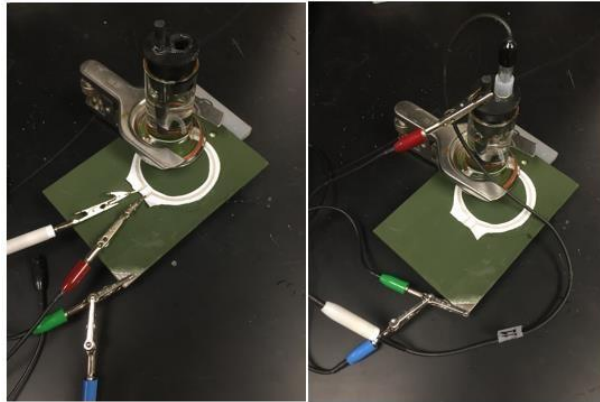


Figure 2: Standard Paint-Cell Setup. (Left) EIS measurements being taken using the sensor utilizing the electrodes on the sensor, (Right) EIS measurements using the saturated calomel reference electrode and graphite rod counter electrode instead of the electrodes on the sensor. This arrangement on the right would constitute a control experiment since the sensor electrodes are not being used.

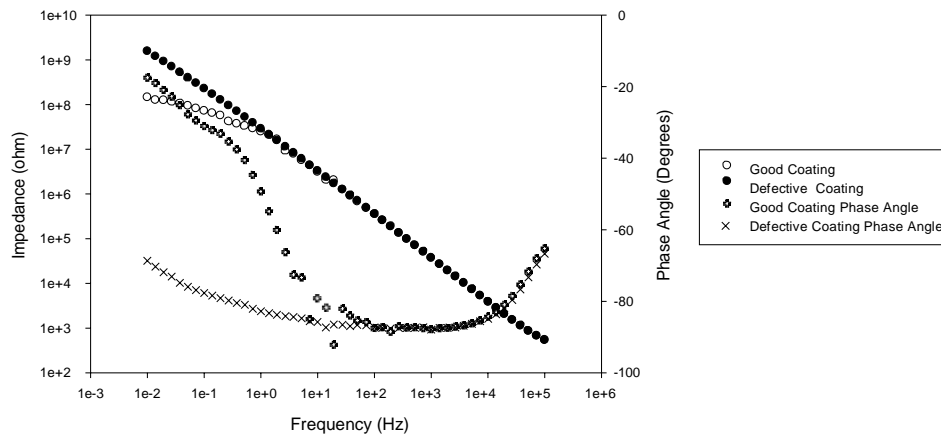


Figure 3: EIS Bode plot comparing sensor-obtained data from a good coating and a coating with an intentional pinhole defect. Full-strength artificial seawater was used for the electrolyte. The sensor's counter and reference electrodes were used, and the working electrode was the bare steel underneath the coating.

REFERENCES:

Kuentzler, M. et al. (2014). "Development of a Thin and Flexible Sensor for Assessing Corrosion Damage of Hard-to-Access Painted Surfaces." *Naval Engineers Journal*, 126(4).

THERMALLY-CONTROLLED BIOPRINTING OF BONE MARROW STEM CELL-LADEN COLLAGEN TYPE – I / PLURONIC F127 COMPOSITE BIOINK FOR BONE TISSUE ENGINEERING

K.K. Moncal¹, A. Akkouch² and I.T. Ozbolat¹

¹The Department of Engineering Science and Mechanics, Pennsylvania State University, University Park, PA-16802, USA

²Dows Institute for Dental Research, University of Iowa, Iowa City, IA-52245, USA

ABSTRACT

Bioprinting of thermally cross-linked hydrogels have gained a great attention in tissue engineering due to their tunable bioprintability. In this paper, we present a new composite bioink made of collagen type-I and Pluronic F127 hydrogels loaded with bone marrow stem cells (BMSCs). We studied bioprintability of the composite bioink to fabricate three dimensional (3D) porous scaffolds for bone tissue regeneration. A thermally-controlled bioprinting unit was used to accurately control the temperature during the flow of the bioink, which was validated using infrared thermography. The composite bioink solution was prepared using combinations of collagen type-I at concentrations of 3 and 6 (mg/ml) and Pluronic F127 hydrogel at concentrations of 40 and 60 % (w/v) with mixing ratio of 1:1, 1:2, 2:1. Bioprintability of composite bioinks were studied using a pneumatically-driven extrusion every 5 minutes for 50 minutes total. We observed how the behavior of the composite bioink changed at every 5 minutes. Cell viability study was performed before and after bioprinting. Although cell viability was impaired during bioprinting, cells were able to recover and proliferate in a week in-vitro culture.

Keywords: Bioprinting, Collagen Type-I, Pluronic F127, Bone Tissue Engineering.

INTRODUCTION

Three dimensional (3D) scaffolds have been widely used in bone tissue regeneration [1]. Bone tissue scaffolds should be biodegradable, biocompatible, and able to support enough mechanical properties to keep the structure maintained in a solid shape until new bone tissue forms [2]. Porosity and pore size are specifically important fabrication parameters for ideal scaffold construction in bone tissue engineering [3, 4]. Bone scaffolds need to have fully interconnected porosity because of enhancing the diffusion of oxygen, transportation of nutrients, and recruitment of progenitor cells during new tissue formation [1, 3, 4].

In the literature, several techniques were studied to fabricate 3D scaffolds for bone tissue regeneration [4]. However, fabrication of bone scaffolds requires a certain pore size, and high pore interconnectivity. Therefore, 3D printing method has recently become an increasingly popular method for bone tissue engineering applications [1, 5, 6]. This technique

is able to control the pore size and filament diameter based on requirements. Computer aided design (CAD) models can be easily printed using layer by layer deposition [6, 7]. This technique is an attractive method to design and fabricate 3D scaffolds because of the reproducibility of the structure [6].

A wide variety of hydrogels, including alginate [8-10], collagen type-I [9-11], fibrin [9, 10], and Pluronic F127 [10] have been used in 3D bioprinting for bone tissue engineering. Collagen type-I hydrogel was shown to facilitate the best bone tissue formation and has the highest gene expression compared to other hydrogels because collagen type-I is the main and the most important organic component of bone tissue extra cellular matrix [10].

Pluronic® F127 mixed with collagen type-I composition was studied for adipogenic differentiation of bone marrow-derived mesenchymal stem cells (MSCs) within 3D hydrogel scaffolds [12]. Pluronic was provided a suitable interaction, and differentiation environment for the cells, and mixing of these two hydrogels increased biological response of MSCs on the composite scaffold [12]. Collagen type-I incorporated with Pluronic enhanced injectability of the composition at room temperature and improved the temperature sensitivity for quick thermo-gelation [13].

To our knowledge, there has been no study on the bioprintability of collagen type-I and Pluronic composite hydrogel solution, where bioprintability of collagen can be controlled by mediating the extrusion kinetics of Pluronic. In this study, we present such a composite bioink loaded with bone marrow stem cells (BMSCs) for bioprinting of bone tissue scaffolds. We studied the bioprintability of the composite bioink through a new custom-made nozzle system and performed viability study of BMSCs. Although cell viability decreased during printing due to shear-stressed induced cell damage, cells were able to recover and proliferate in a week in-vitro culture.

RESULTS and DISCUSSIONS

As shown in Fig. 1(A), the MABP was placed in a biosafety cabinet for sterilization purposes, where TCBU components were mounted on one of the arms of the MABP (see Fig. 1(B)). The composite bioink was prepared by mixing 6

(mg/ml) of collagen type-I and 60% (w/v) Pluronic with a mixing ratio of 1:1. The bioink composition was extruded through the glass pipette pneumatically (see Fig. 2(A)) and thermal images were taken to validate the temperature of the extrusion process, where the temperature at the end of the nozzle tip was obtained as $37\pm 2^\circ\text{C}$ (see Fig. 2(B)). Ten layers of 3D porous scaffold was successfully bioprinted with collagen fibers extruded within Pluronic hydrogel onto a heated plate (see Fig. 2(C)). Trypan blue method was used to check cell viability. Cell viability was calculated as $98.61\pm 1.21\%$ and $92\pm 1.68\%$ ($n=3$) (see Fig. 3(A)) before and right after bioprinting, respectively.

Although, cell viability results showed minimum cell damage during the bioprinting process, the shear stress on cells resulted in necrosis that was obvious a day after and cell viability dropped to $72.92\pm 9.1\%$ ($n=3$). Cell viability; however, increased to $83.97\pm 0.64\%$ ($n=3$) on day 7 due to the proliferation of cells (see Fig. 3(A)). Figures 3(B-D) show printed cells in micro-extruded filaments in different magnification (4 to 20X), where cells were uniformly distributed within micro-filaments.

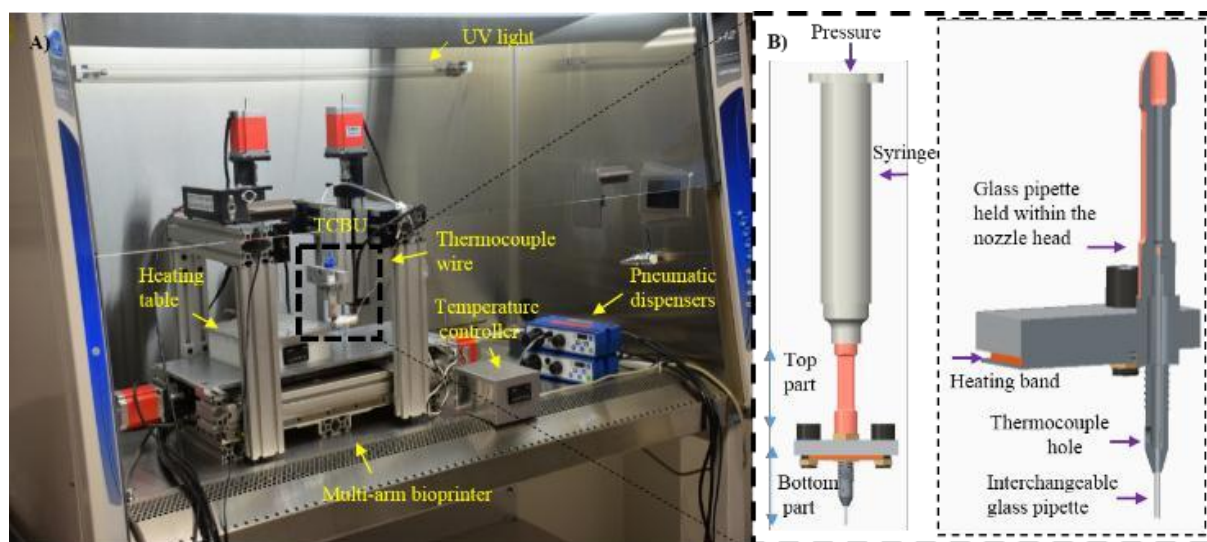


Figure 1. (A) Multi-arm Bioprinter inside a biosafety cabinet, (B) thermally-controlled extrusion unit and its components.

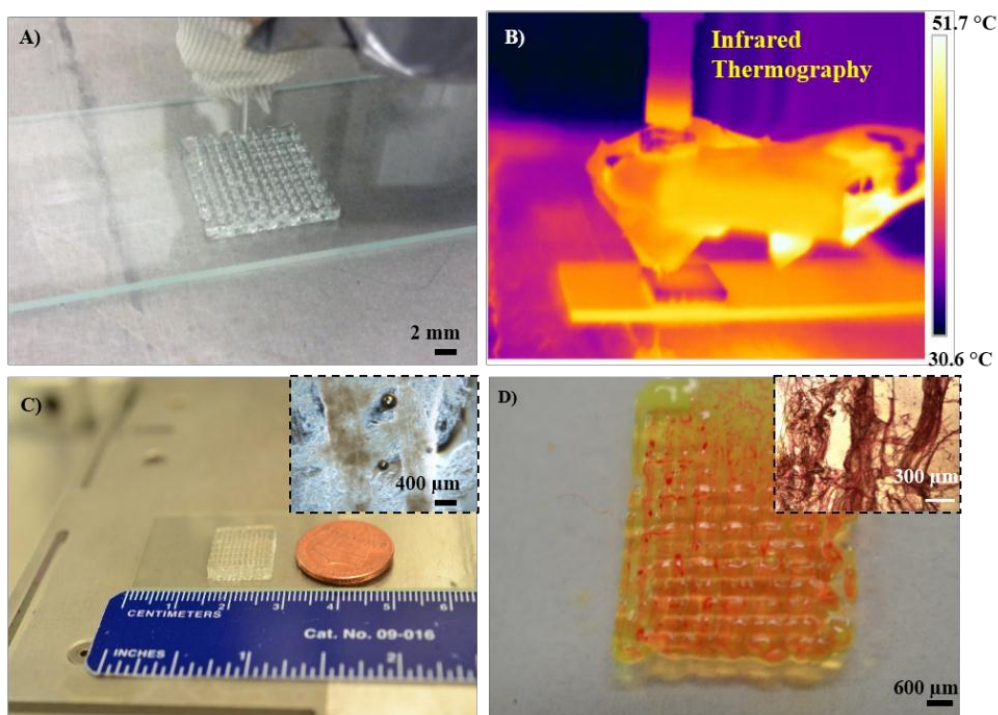


Figure 2. (A) 3D Bioprinting in action, (B) an IR image showing the temperature map of the extrusion unit, (C) a bioprinted scaffold and demonstration of collagen type-I fibers within the bioprinted scaffold, (D) a bioprinted scaffold stained with picosirius red for visualization of collagen type-I fibers.

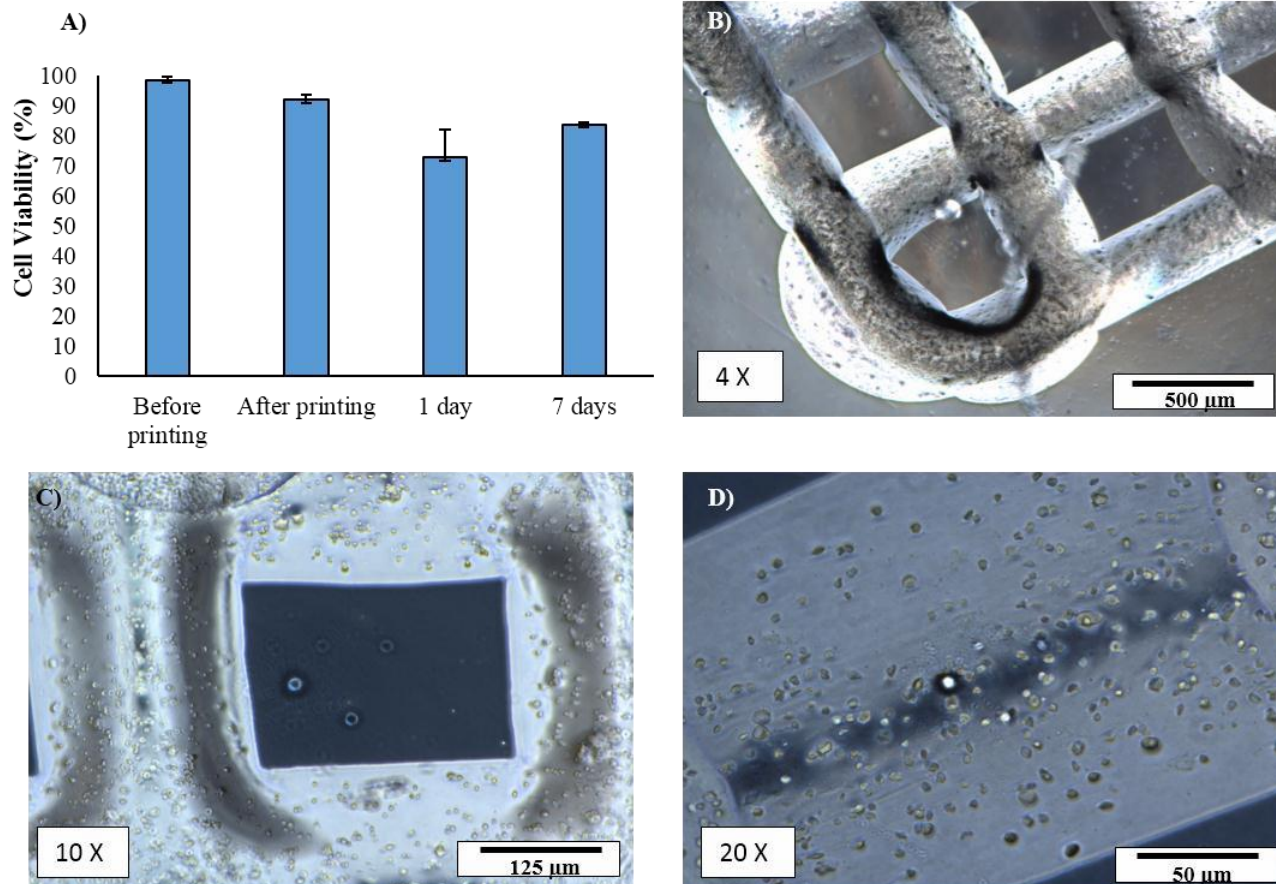


Figure 3. (A) Result of bioprinting process on cell viability, (B) bioprinted scaffold was visualized under an inverted microscope with (4X) magnification, (C) scaffold pore with (10X) magnification, (D) high resolution scaffold filament with rounded cells with (20X) magnification.

References

1. Bose, S., S. Vahabzadeh, and A. Bandyopadhyay, Bone tissue engineering using 3D printing. *Materials Today*, 2013. **16**(12): p. 496-504.
2. Rezwani, K., et al., Biodegradable and bioactive porous polymer/inorganic composite scaffolds for bone tissue engineering. *Biomaterials*, 2006. **27**(18): p. 3413-3431.
3. Park, S., S. Lee, and W. Kim, Fabrication of porous polycaprolactone/hydroxyapatite (PCL/HA) blend scaffolds using a 3D plotting system for bone tissue engineering. *Bioprocess and Biosystems Engineering*, 2011. **34**(4): p. 505-513.
4. Loh, Q.L. and C. Choong, Three-dimensional scaffolds for tissue engineering applications: role of porosity and pore size. *Tissue Eng Part B Rev*, 2013. **19**(6): p. 485-502.
5. Liu Tsang, V. and S.N. Bhatia, Three-dimensional tissue fabrication. *Advanced Drug Delivery Reviews*, 2004. **56**(11): p. 1635-1647.
6. Giannitelli, S.M., et al., Current trends in the design of scaffolds for computer-aided tissue engineering. *Acta Biomaterialia*, 2014. **10**(2): p. 580-594.
7. Sun, W., et al., Computer-aided tissue engineering: overview, scope and challenges. *Biotechnology and Applied Biochemistry*, 2004. **39**(1): p. 29-47.
8. Fedorovich, N.E., et al., Three-dimensional fiber deposition of cell-laden, viable, patterned constructs for bone tissue printing. *Tissue Engineering Part A*, 2008. **14**(1): p. 127-133.
9. Weinand, C., et al., Comparison of hydrogels in the in vivo formation of tissue-engineered bone using mesenchymal stem cells and beta-tricalcium phosphate. *Tissue engineering*, 2007. **13**(4): p. 757-765.
10. Weinand, C., et al., Hydrogel- β -TCP scaffolds and stem cells for tissue engineering bone. *Bone*, 2006. **38**(4): p. 555-563.
11. Inzana, J.A., et al., 3D printing of composite calcium phosphate and collagen scaffolds for bone regeneration. *Biomaterials*, 2014. **35**(13): p. 4026-4034.
12. Vashi, A.V., et al., Adipose differentiation of bone marrow-derived mesenchymal stem cells using

Pluronic F-127 hydrogel in vitro. *Biomaterials*, 2008. **29**(5): p. 573-579.

13. Fu, C., et al., Effects of collagen incorporation on thermogelation and hydrogel characteristics of aqueous Pluronic F127 copolymer system. *Colloid and Polymer Science*, 2015. **293**(8): p. 2191-2200.

BiT-Starch Ultrasonic Transducers

Leland Tien, Janet Xu, and Bernhard R. Tittmann

**Department of Engineering Science and Mechanics
The Pennsylvania State University
University Park, PA 16802**

ABSTRACT

Ultrasonic nondestructive evaluation (UNDE) can provide real time flaw detection in metal piping. The nuclear power industry has expressed great interest in using this technology, but a number of issues prevented its use. Traditional ferroelectrics degrade quickly at the high temperatures present in a nuclear power plant. Our research has focused on Bismuth Titanate (BiT), a high Curie temperature ferroelectric that can withstand these higher temperatures. Recently, a spray-on method has been developed using a powder loaded Sol to deposit a BiT-Sol composite onto the surface of various substrates, such that it can be used as an ultrasonic transducer. However, this caused issues with corrosion on carbon steel (a material frequently found in nuclear power plants), so we have replaced the Sol with a potato starch binder to form lead free high temperature tolerant thick film transducers, and it does not encounter the corrosion problems that occurred when using the BiT-Sol composite.

Verification of a Fluid-Structure Interaction Solver

Nicholas Labarbera

Department of Engineering Science and Mechanics, Penn State, PA-16802, USA

As fluid-structure interaction codes become more prevalent, there is a growing need to properly verify if the numerics of the codes are correctly implemented. There are well established methods for verifying single phase solvers in both computational fluid dynamics and structural dynamics [1, 2]. One of the most common methods is to perform a systematic grid study and examine the convergence rates of errors. However, there is much less literature on methods to verify multi-phase flows such as fluid-structure interaction codes.

One of the hurdles to verification of fluid-structure interaction codes is the difficulty in deriving an analytic solution. But even if the analytic solution is known, there is disagreement in the literature as to how errors should be calculated and compared to theoretical convergence rates. These problems are often a result of the difficulty in defining error metrics on deforming Eulerian grids.

The goal of this research was meant to answer the question:

“What error metric should be used for FSI verification and what would be the expected rate of convergence when the fluid and solid solvers are different orders?”

For example, what is the expected rate

of convergence when the fluid solver is order 2 and the solid solver is order 3? By trying to answer these questions, we have developed a technique to help carry out verification of fluid-structure interaction codes. Specifically, this work focuses on the development of a framework for the verification of partitioned fluid-structure interaction solvers. We aimed to provide as general a framework as possible. A few goals were a method that is independent of domain geometries and is well suited for partitioned solvers by having the capability to verify unequal order solvers. This work also tries to bring attention to some of the mistakes that can be made in the definition of an error metric to use for a grid study for a fluid-structure interaction solver.

References

- [1] P. J. Roache, “Quantification of uncertainty in computational fluid dynamics,” *Annual Review of Fluid Mechanics*, vol. 29, no. 1, pp. 123–160, 1997.
- [2] W. L. Oberkampf and F. G. Blottner, “Issues in computational fluid dynamics code verification and validation,” *AIAA journal*, vol. 36, no. 5, pp. 687–695, 1998.

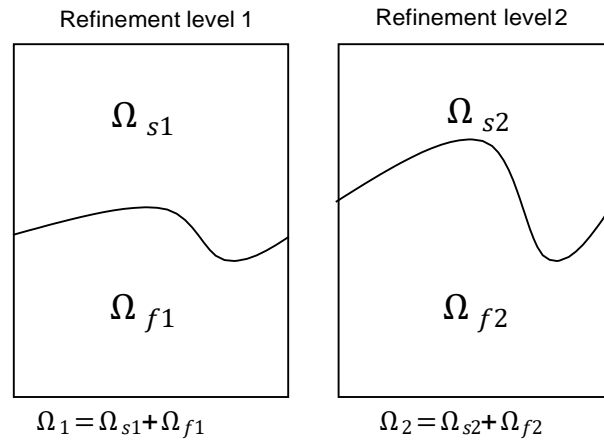


Figure 1: Example demonstrating the difficulty in defining a metric for the fluid in the deformed configuration. For this example, how would one define the metric between the two fluid domains? L_p metrics are defined as integrals over a domain, in the form $\int_{\Omega} \|\mathbf{u}_{f1} - \mathbf{u}_{f2}\|^p dx$, but what does Ω equal? If $\Omega = \Omega_{f1}$ then not all of Ω_{f2} is represented. If $\Omega = \Omega_{f2}$ then \mathbf{u}_{f1} in the integrand is undefined for $\Omega_{f2} \setminus \Omega_{f1}$.

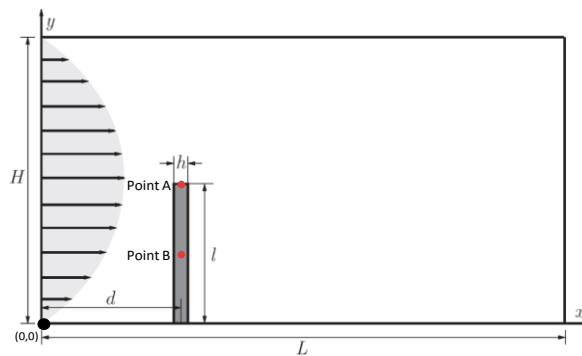


Figure 2: Schematic of test case used for verifying the FSI solver. This case consists of a flexible beam perpendicular to channel flow. The incoming fluid displaces the beam

DEVELOPMENT OF VAPOR-DEPOSITED SACRIFICIAL MAGNESIUM COATING FOR THE PROTECTION OF AEROSPACE ALLOYS

Department of Engineering Science and Mechanics

Robert Gresh and Barbara Shaw

Magnesium thin films produced via physical vapor deposition show properties that make them promising coating candidates. It has been shown that thin film magnesium alloys can be more electrochemically active than bulk magnesium alloys. This appears to be an effect of the microstructure and purity of the thin films, both of which can be controlled using deposition techniques. This research explores the effect of microstructure on the corrosion potential and corrosion properties of thin film magnesium alloys. The microstructure can be altered by thin film parameters such as deposition rate, angle of incidence, temperature, substrate rotation, energy of vapor ions, and film thickness. Thin films with lower corrosion potentials and lower corrosion rates than bulk magnesium could be used as a sacrificial corrosion coating for structural magnesium alloys.

Developing a magnesium thin film with a lower open circuit potential than magnesium is difficult because magnesium is one of the most active metals on the galvanic series [1,2]. Evaporation and sputtering techniques can be used to produce thin films with lower open circuit potential than bulk magnesium alloys. These deposition techniques can produce high purity films (as impurities in the target material may not deposit as easily as magnesium), provide unique solid solution stoichiometry that may not be possible in cast alloys, and produce materials with different microstructures than bulk alloys. This study focuses on the development of a novel sacrificial layer for the corrosion protection of commercially available Mg alloys by studying magnesium

thin films deposited via electron beam physical vapor deposition (EBPVD) and biased target deposition (BTD).

Vapor deposited magnesium thin films show a decreasing corrosion potential with increasing angle, but do not have desirable corrosion resistance properties. Films were produced at fixed angles via EBPVD and BTD (Table 1). Some films were deposited at a fixed angle and others were rotated during deposition. Polarization resistance and electrochemical impedance spectroscopy (EIS) were performed in 0.1M NaCl solution to determine the corrosion rates of thin-film specimens. The compositions of the thin-film samples were determined using energy-dispersive X-ray spectroscopy (EDS) to identify impurities. Film morphologies were characterized with a field-emission scanning electron microscope (FE-SEM) (Figure 1). The microstructure of the thin films was analyzed using Grazing Incidence X-Ray Diffraction (GIXRD) to determine the phases present in each sample. The results of this analyses will be summarized and the development of magnesium thin films into a sacrificial coating for magnesium alloys will be discussed.

Table 1. Deposition parameters of deposited thin films. All films were deposited at ambient temperature with a base pressure of 3.8E-6, except for the BTD S2 sample which was deposited via BTD at a base pressure of 6.56E-4.

| Film ID | Deposition Angle (degrees) | Target Deposition Rate (Å/s) | Thickness (µm) |
|---------|----------------------------|------------------------------|----------------|
| M612 | 0 | 8 | 0.740 |
| M515 | 0 | 20 | 1.920 |
| M614 | 45 | 20 | 1.758 |
| M615 | 60 | 20 | 3.528 |
| M516 | 78 | 20 | 11.860 |
| M517 | 85 | 20 | 8.240 |
| BTD S2 | 0 | 1 | 0.934 |

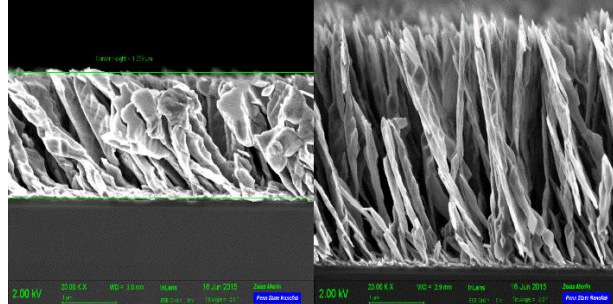


Figure 1. FESEM images of Pure Mg thin films. The films were deposited at 45° (left, M5614) and 60° (right, M615). Both films were deposited at 20 Å/s and to a target thickness of 1µm. The 60° film was much thicker (3.528µm) due to the formation of thin blades during growth. Both films show a preferred orientation.

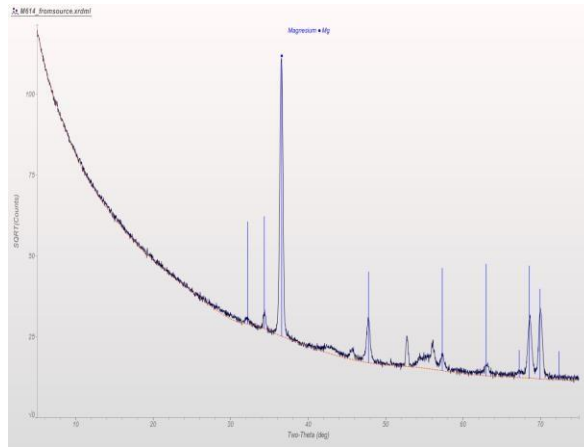


Figure **Error! No text of specified style in document.** XRD pattern of pure Mg thin film, M614, deposited at 45°. The pattern matches a Mg diffraction pattern with the dominant peak is the 101 peak. This pattern was measured parallel to the direction of vapor flux.

References

1. B. L. Mordike and T. Ebert, “Magnesium Properties — applications — potential,” *Materials Science and Engineering*, vol. 302, pp. 37-45, 2001.
2. K. Guo, “A review of magnesium/magnesium alloys corrosion and its protection,” *Recent Patents on Corrosion Science*, vol. 2, pp. 13-21, 2010.

Multiple stiffening effects of nano-scale knobs on human red blood cells infected with *Plasmodium falciparum* malaria parasite

Yao Zhang and Sulin Zhang

Department of Engineering Science and Mechanics, The Pennsylvania State University,
University Park, PA 16802, USA

Plasmodium falciparum (*Pf*) is the most virulent human malaria parasite, causing approximately 700,000 deaths each year (1). Following entry into RBCs, the parasite matures through the ring (0-24 h), trophozoite (24-36 h), and schizont stages (40-48 h). This intra-erythrocyte maturation is accompanied by striking changes in the surface topography and membrane architecture of the infected RBC (2). A notable modification is the formation of nano-scale protrusions, commonly known as knobs, at the RBC surface during the second half (24-48 h) of the asexual cycle. These protrusions mainly comprise the knob-associated histidine-rich protein (KAHRP) and the membrane-embedded cytoadherence protein, *Pf*-infected erythrocyte membrane protein 1 (PfEMP1). KAHRP binds to the fourth repeat unit of the spectrin α -chain, to ankyrin, to spectrin-actin-protein 4.1 complexes, and to the cytoplasmic domain of PfEMP1. These attachments enhance the vertical coupling between the lipid bilayer and the spectrin network. Another striking modification in the *Pf*-infected RBC membrane is the reorganization of the cytoskeletal network caused by parasite-induced actin remodeling. As a result of these molecular level modifications, the *Pf*-infected RBC exhibits markedly increased stiffness (the shear modulus increases on average from $\sim 4\text{--}10\ \mu\text{N/m}$ in normal/uninfected RBCs, to $\sim 40\ \mu\text{N/m}$ at the trophozoite stage, and to as high as $90\ \mu\text{N/m}$ at the schizont stage (3)) and cytoadherence to the vascular endothelium, which enable sequestration from circulation in vasculature, and evasion from the surveillance mechanisms of the spleen. Although *in vitro* experimental studies have revealed roles of particular parasite-

encoded proteins in remodeling the host RBC, the mechanism by which *Pf*-infected RBCs gain dramatically increased stiffness has remained unclear. Indeed, uncertainty remains as to whether the loss of deformability arises from the structural reorganization of the host membrane components or from the deposition of parasite proteins. That is, it is not clear whether the stiffening is due to remodeling of the spectrin network, or to the formation of the knobs, or both. As experimental studies alone have heretofore not been able to determine the molecular details, numerical modeling, combined with a variety of experimental observations and measurements, offers an alternative approach to reveal the underlying mechanisms.

We present here a coarse-grained (CG) molecular dynamics (MD) RBC membrane model to correlate structural modifications at the molecular ultrastructure level with the shear responses of the *Pf*-infected RBC membrane, focusing on the second half of the parasite's intra-RBC asexual cycle (24–48 h), i.e. the trophozoite and schizont stages. The CG model is computationally efficient, and able to capture the molecular structures of the RBC membrane in both normal and infected states. CGMD simulations reveal that spectrin network remodeling accounts for a relatively small change in shear modulus. Instead, the knobs stiffen the membrane by multiple mechanisms, including composite strengthening, strain hardening, and knob density-dependent vertical coupling. Our findings provide molecular-level understanding of the stiffening mechanisms operating in *Pf*-infected RBCs, and shed light on the pathogenesis of falciparum malaria.

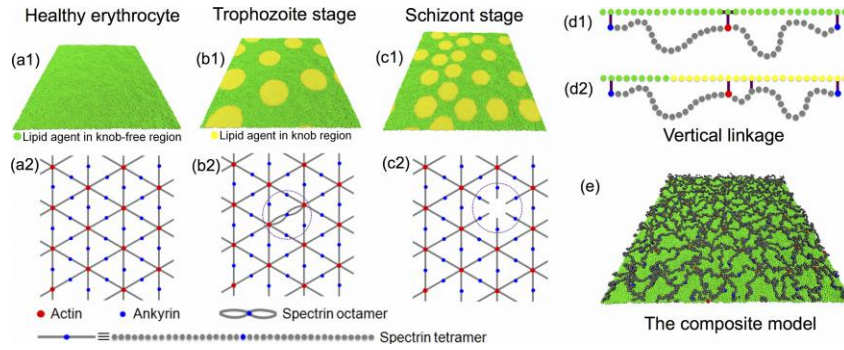


Fig. 1. A composite CG model of the human RBC membrane. (a)-(c) The one-agent-thick lipid bilayer model and the spectrin network model for uninfected (a1, a2), trophozoite-stage (b1, b2) and schizont-stage (c1, c2) RBCs, respectively. (d) Vertical associations between the overlying lipid bilayer and the spectrin network in normal (d1) and *Pf*-infected (d2) membranes. (e) The composite CG model integrating the lipid bilayer and the spectrin network. Green: normal lipid agents; yellow: lipid agents representing the knobby region; red: actin oligomers; blue: ankyrins; and grey: spectrin beads.

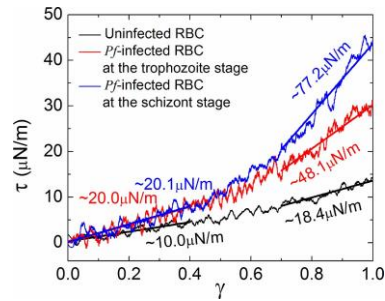


Fig. 2. Shear stress-strain responses of uninfected (black line) and *Pf*-infected RBC membranes at the trophozoite (red line) and schizont (blue line) stages.

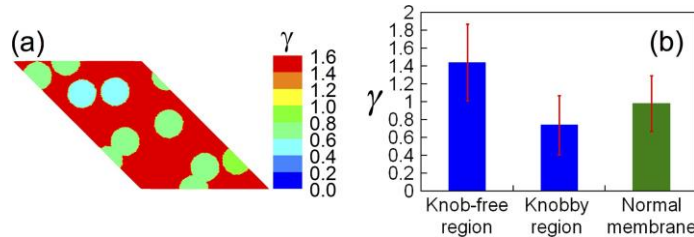


Fig. 3. Stiffening due to the inhomogeneous strain induced by the presence of the knobs ($\alpha = 0.35$). (a) Inhomogeneous shear strain distribution in the spectrin network. The shear strain in the knob-free regions is much higher than that applied, representing a stiffening mechanism due to the strain-hardening property of the spectrin network. (b) The average shear strain in the knob-free regions is $\gamma_F = 1.44$, while that in the knobby regions is $\gamma_K = 0.74$ at an applied shear strain $\gamma_C = 1$. The shear strain in the normal spectrin network (without knobs) is homogeneous and consistent with the applied shear strain.

Reference

1. Murray CJL, *et al.* (2012) Global malaria mortality between 1980 and 2010: a systematic analysis. *Lancet* 379(9814):413-431.
2. Maier AG, Cooke BM, Cowman AF, & Tilley L (2009) Malaria parasite proteins that remodel the host erythrocyte. *Nat Rev Micro* 7(5):341-354.
3. Suresh S (2006) Mechanical response of human red blood cells in health and disease: some structure-property-function relationships. *J Mater Res* 21(08):1871.